Monthly Notices
of the
ROYAL ASTRONOMICAL SOCIETY

Mon. Not. R. Astron. Soc. **415,** 545–562 (2011) doi:10.1111/j.1365-2966.2011.18725.x

Dynamical masses of early-type galaxies: a comparison to lensing results and implications for the stellar initial mass function and the distribution of dark matter

J. Thomas,[1,2]⋆ R. P. Saglia,[1,2] R. Bender,[1,2] D. Thomas,[3] K. Gebhardt,[4] J. Magorrian,[5] E. M. Corsini,[6] G. Wegner[7] and S. Seitz[1,2]

[1] *Universitätssternwarte München, Scheinerstraße 1, D-81679 München, Germany*
[2] *Max-Planck-Institut für Extraterrestrische Physik, Giessenbachstraße, D-85748 Garching, Germany*
[3] *Institute of Cosmology and Gravitation, University of Portsmouth, Dennis Sciama Building, Burnaby Road, Portsmouth PO1 3FX*
[4] *Department of Astronomy, University of Texas at Austin, C1400, Austin, TX 78712, USA*
[5] *Theoretical Physics, Department of Physics, University of Oxford, 1 Keble Road, Oxford OX1 3NP*
[6] *Dipartimento di Astronomia, Università di Padova, vicolo dell'Osservatorio 2, I-35122 Padova, Italy*
[7] *Department of Physics and Astronomy, 6127 Wilder Laboratory, Dartmouth College, Hanover, NH 03755-3528, USA*

Accepted 2011 March 15. Received 2011 March 15; in original form 2010 July 9

ABSTRACT

This work aims to study the distribution of the luminous and dark matter in Coma early-type galaxies. Dynamical masses obtained under the assumption that mass follows light do not match with the masses of strong gravitational lens systems of similar velocity dispersions. Instead, dynamical fits with dark matter haloes are in good agreement with lensing results. We derive mass-to-light ratios of the stellar populations from Lick absorption line indices, reproducing well the observed galaxy colours. Even in dynamical models with dark matter haloes the amount of mass that follows the light increases more rapidly with the galaxy velocity dispersion than expected for a constant stellar initial mass function (IMF). While galaxies around $\sigma_{\rm eff} \approx 200\,{\rm km\,s^{-1}}$ are consistent with a Kroupa IMF, the same IMF underpredicts luminous dynamical masses of galaxies with $\sigma_{\rm eff} \approx 300\,{\rm km\,s^{-1}}$ by a factor of 2 and more. A systematic variation in the stellar IMF with the galaxy velocity dispersion could explain this trend with a Salpeter IMF for the most massive galaxies. If the IMF is instead constant, then some of the dark matter in high-velocity-dispersion galaxies must follow a spatial distribution very similar to that of the light. A combination of both, a varying IMF and a component of dark matter that follows the light is possible as well. For a subsample of galaxies with old stellar populations, we show that the tilt in the Fundamental Plane can be explained by systematic variations of the total (stellar + dark) mass inside the effective radius. We tested commonly used mass estimator formulae, finding them accurate at the 20–30 per cent level.

Key words: galaxies: elliptical and lenticular, cD – galaxies: kinematics and dynamics – galaxies: structure.

1 INTRODUCTION

The masses of galaxies are revealed by the gravitational interaction of their matter constituents, for example, by stellar or gas kinematics or gravitational lensing effects. The caveat is that these effects rigorously constrain only the total amount of the gravitating mass. The decomposition into luminous and dark matter relies on further assumptions. For example, in dynamical studies of early-type galaxies, it is commonly assumed that the stellar mass distribution follows the light. Any radial increase in the mass-to-light ratio – if needed to explain the observed velocities of the stars – is attributed to dark matter.

The limitation of this approach becomes clear if one imagines a galaxy dark matter halo that follows the light distribution exactly. Discriminating between luminous and dark matter according to their potentially different radial distributions would fail in this case. In fact, there would be no direct way to dynamically unravel the relative contributions of luminous and dark matter to the galaxy mass. It is unlikely that a real galaxy halo follows the light distribution exactly, yet it exemplifies the intrinsic degeneracies in any mass decomposition. On top of this, even the most advanced present-day dynamical

---

⋆E-mail: jthomas@mpe.mpg.de

modelling techniques rely on symmetry assumptions and, often, on the assumption of a steady-state dynamical system. If the symmetry assumptions are strongly violated, dynamical mass-to-light ratios can be biased by a factor of up to 2 (Thomas et al. 2007a).

To cross-check the validity of the assumptions in dynamical modelling, it is important to compare the resulting masses with other independent methods. *Total* masses can be most directly compared to results from gravitational lensing, which is the first goal of this paper.

An examination of the mass *decomposition* requires the investigation of a galaxy's stellar population. Since the latter provides an independent measure of the stellar mass-to-light ratio, the comparison of dynamical and stellar population masses yields further constraints on the dark matter content. In the above-mentioned case, for example, the dynamical mass-to-light ratio, $\Upsilon_{*,\mathrm{dyn}}$, would exceed the corresponding stellar population value, indicating that some fraction of the galaxy's mass is actually dark matter.

Unfortunately, stellar population models do not provide unique stellar mass-to-light ratios. They suffer from an incomplete knowledge of the stellar initial mass function (IMF), as well as age–metallicity degeneracies. Observations in and around our own Galaxy indicate that the IMF slope flattens below $0.5\,\mathrm{M}_{\odot}$ (Scalo 1986; Kroupa 2001). Recent spectroscopic observations of massive ellipticals in the near-infrared point towards the low-mass slope of the IMF in these galaxies, being steeper (van Dokkum & Conroy 2010). Yet, until now the IMF in distant galaxies with unresolved stellar populations remains largely uncertain. This translates into a significant indeterminacy of population mass-to-light ratios: the steeper the slope at the low-mass end, the higher the population mass-to-light ratio. Hence, the stellar population approach is not directly conclusive as a probe of the mass decomposition in dynamical models.

Conversely, if dynamical stellar mass determinations were free of ambiguities with respect to a dark matter contamination, then they could serve as a measure for the slope of the IMF in distant galaxies. The method would be to tweak the IMF in the stellar population models until agreement with the dynamical stellar masses is achieved.

The ambiguities in both, dynamical stellar masses and stellar population models, make neither of the approaches directly applicable. Nevertheless, comparing dynamical with stellar population models is important to (1) narrow down the dynamically plausible range of possible IMFs; and (2) delimit the range of dark matter fractions compatible with observed stellar population properties. This is the second goal of this paper in which we compare dynamical and stellar population masses in a sample of 16 Coma early-type galaxies.

Our dynamical models account for both the full variety of possible orbit configurations in axisymmetric, flattened galaxies and dark matter. In this respect, we extend previous studies. Cappellari et al. (2006), for example, used a similar modelling technique to compare dynamical and stellar population masses in the SAURON sample, but they did not consider dark matter explicitly in their dynamical models. The justification for this neglect was the expected insignificance of the dark matter in the central galaxy regions probed by the SAURON observations ($r_{\mathrm{obs,max}} \lesssim r_{\mathrm{eff}}$). However, measuring only the sum of luminous and dark masses makes the comparison with stellar population models potentially uncertain. Napolitano, Romanowsky & Tortora (2010) analysed a large sample of early-type galaxies taking into account the contribution from dark matter, but their models do not account for galaxy flattening and rotation.

A subsample of the Coma galaxies was recently analysed by Grillo & Gobat (2010). While they used multiband photometry to derive stellar population properties, our approach is to measure ages, metallicities and [α/Fe] ratios from Lick indices to reduce potential biases in population parameters. Likewise, the analysis of SLACS galaxies by Treu et al. (2010), combining constraints from gravitational lensing and stellar dynamics, relied on multiband photometry for the stellar population part.

Mass-to-light ratios of early-type galaxies are of particular interest to understand the tilt of the Fundamental Plane (FP). Virial relations imply that the effective surface brightness $\langle I \rangle_{\mathrm{eff}}$, the effective radius, r_{eff}, and the central velocity dispersion, σ_0, in hot stellar systems are not independent of each other. This is revealed by the FP of early-type galaxies (Djorgovski & Davis 1987; Dressler et al. 1987). Yet, the observed FP is tilted with respect to the simple case of a virialized, homologous family of dynamical systems. This tilt can reflect (1) systematic variations in the luminosity distribution (e.g. Saglia, Bender & Dressler 1993; Trujillo, Burkert & Bell 2004); (2) systematic variations in the orbital structure (e.g. Ciotti, Lanzoni & Renzini 1996); or (3) systematic variations in the mass-to-light ratio, as a result of varying stellar populations and/or dark matter distributions (e.g. Renzini & Ciotti 1993). Understanding these variations allows a deeper insight into the formation process of early-type galaxies (Bender, Burstein & Faber 1992).

Most of the above-mentioned effects can be factored out if additional information about the stellar populations and/or the mass distributions is available. Aperture spectroscopy is one way to measure stellar population properties. By assuming simple scaling laws, it can also provide estimates for dynamical masses, such that the contributions of stellar population and dynamical effects on the FP tilt can be disentangled (e.g. Hyde & Bernardi 2009; Graves & Faber 2010). More reliable constraints come from the radially resolved spectroscopy and detailed dynamical (or lensing) models of galaxies (e.g. Cappellari et al. 2006; Bolton et al. 2007). The third goal of this paper is to follow the latter approach and to use the specific information contained in our two-component dynamical models for further investigation into the origin of the FP tilt.

This paper is organized as follows. Section 2 reviews the galaxy sample and models. In Section 3, we compare projected masses from dynamical models and from gravitational lensing against each other. Section 4 deals with the comparison of luminous dynamical and stellar population masses. The dark matter distribution is analysed in Section 5 and implications for the tilt of the FP are addressed in Section 6. This paper is summarized in Section 7.

2 GALAXY SAMPLE AND MODELLING

The sample analysed in this paper comprises 16 Coma early-type galaxies in the luminosity range $M_B = -19.88$ to -22.26 (eight giant ellipticals and eight lenticular/intermediate-type galaxies). It is almost identical to the sample presented in Thomas et al. (2009b). Only the galaxy GMP3958 has been omitted for its strong gas emission, which hampers reliable stellar population modelling.

For the dynamical analysis of each galaxy, a composite of the ground-based and *HST* photometry has been used. Stellar absorption line data for the kinematics and Lick indices come from various long-slit spectra, at least along the major-axis and minor-axis, but in many cases covering other position angles as well. The spectra extend to 1–4r_{eff}. Details about the photometric and spectroscopic data have been published in Mehlert et al. (2000), Wegner et al. (2002), Corsini et al. (2008) and Thomas et al. (2009b).

2.1 Dynamical modelling

To the kinematic and photometric data, we applied our implementation of Schwarzschild's orbit superposition technique (Schwarzschild 1979) for axisymmetric potentials (Richstone & Tremaine 1988; Gebhardt et al. 2003; Thomas et al. 2004, 2005a). A detailed description of the models is given in Thomas et al. (2007b). Most important for this paper are the assumptions about the mass structure. We will consider two sets of models. For the first set, it is assumed that all the mass follows the light, that is,

$$\rho = \Upsilon \times \nu \tag{1}$$

where ν is the three-dimensional luminosity density. By construction, the mass-to-light ratio, Υ, here includes the contribution of both the stellar mass and the dark mass of a galaxy. It is not known in advance and obtained by a χ^2-minimization with respect to the kinematical observations. The best-fitting Υ of one-component (i.e. self-consistent) models will be referred to as $\Upsilon_{*,\mathrm{sc}}$ in the remainder of this paper and can be found in Table 1.

For the second and standard set of models, we assume a mass density of the form

$$\rho = \Upsilon \times \nu + \rho_{\mathrm{DM}}. \tag{2}$$

The first component again follows the light, while the second one, ρ_{DM}, accounts for dark matter. Equation (2) is designed to separate the contributions of luminous and dark matter to the total mass of a galaxy. Our basic assumption is that the best-fitting Υ of two-component models represents only the stellar mass of a galaxy and we will refer to it as the dynamical stellar mass-to-light ratio, $\Upsilon_{*,\mathrm{dyn}}$, in the following. Strictly speaking, $\Upsilon_{*,\mathrm{dyn}}$ measures all the mass which follows the light distribution, be it stellar or be it dark matter. In this respect, $\Upsilon_{*,\mathrm{dyn}}$ provides only an upper limit for the stellar mass. As soon as there are other mass components which – for whatever reason – follow the light, they will contribute to $\Upsilon_{*,\mathrm{dyn}}$ as well and the actual galaxy stellar mass-to-light ratio will be smaller than $\Upsilon_{*,\mathrm{dyn}}$. A more detailed discussion upon this issue will be given in Sections 4.4 and 5.2.

According to equation (2), the cumulative (spherical) dark matter fraction, $f_{\mathrm{DM,dyn}}$, of the models inside radius r is

$$f_{\mathrm{DM,dyn}}(r) \equiv \frac{M_{\mathrm{DM,dyn}}(r)}{M_{\mathrm{tot,dyn}}(r)} = \frac{M_{\mathrm{DM,dyn}}(r)}{\Upsilon_{*,\mathrm{dyn}}\, L(r) + M_{\mathrm{DM,dyn}}(r)}, \tag{3}$$

where $M_{\mathrm{tot,dyn}}$, $M_{\mathrm{DM,dyn}}$ and L stand for the cumulative total mass, dark mass and light inside radius r, respectively. Table 1 lists the observationally derived dark matter fractions. Here we consider mostly the region inside r_{eff}, where the average dark matter fraction is $\langle f_{\mathrm{DM,dyn}} \rangle = 23 \pm 17$ per cent, but our data reach out to radii where the stellar and the dark matter densities become equal (Thomas et al. 2007b).

Table 1. Dynamical parameters of Coma galaxies. Columns (1) and (2): galaxy identification (GMP from Godwin, Metcalfe & Peach 1983). Column (3): best-fitting dynamical $\Upsilon_{*,\mathrm{dyn}}$ (R band) in models that explicitly account for dark matter. (The quoted errors include all models that deviate by less than $\Delta\chi^2 \leq 1$ from the best-fitting model. For a more detailed discussion of the errors, the reader is referred to Thomas et al. 2005a.) Column (4): best-fitting dynamical $\Upsilon_{*,\mathrm{sc}}$ (R band), assuming that all the mass follows the light. [According to fig. 2 in Thomas et al. (2007b), the formal errors on $\Upsilon_{*,\mathrm{sc}}$ are smaller than those of $\Upsilon_{*,\mathrm{dyn}}$. However, since the assumption that mass follows light does not yield satisfactory fits to the kinematics, we do not give errors for $\Upsilon_{*,\mathrm{sc}}$ here.] Column (5): dark matter fraction, $f_{\mathrm{DM,dyn}}$, within r_{eff}. Column (6): galaxy velocity dispersion σ_{eff} (inside r_{eff}). Columns (7) and (8): stellar population mass-to-light ratios for the Kroupa IMF (Υ_{Krou}; R band) and Salpeter IMF (Υ_{Salp}; R band), respectively. The mass-to-light ratios are light-weighted averages within r_{eff}. Only radii with a stellar population age $\tau \leq 14$ Gyr are considered.

Galaxy		$\Upsilon_{*,\mathrm{dyn}}$	$\Upsilon_{*,\mathrm{sc}}$	$f_{\mathrm{DM,dyn}}$	σ_{eff}	Υ_{Krou}	Υ_{Salp}
GMP	NGC/IC	($\mathrm{M}_\odot/L_{R,\odot}$)	($\mathrm{M}_\odot/L_{R,\odot}$)		(km s^{-1})	($\mathrm{M}_\odot/L_{R,\odot}$)	($\mathrm{M}_\odot/L_{R,\odot}$)
(1)	(2)	(3)	(4)	(5)	(6)	(7)	(8)
0144	4957	4.50 ± 0.50	7.00	$0.30^{+0.10}_{-0.05}$	211.8 ± 0.4	3.03 ± 0.17	4.74 ± 0.26
0282	4952	5.00 ± 0.50	6.50	$0.25^{+0.13}_{-0.05}$	268.2 ± 0.5	3.57 ± 0.22	5.58 ± 0.34
0756	4944	2.60 ± 0.20	3.00	$0.11^{+0.05}_{-0.05}$	193.2 ± 0.3	1.40 ± 0.06	2.19 ± 0.10
1176	4931	2.00 ± 0.20	2.50	$0.31^{+0.05}_{-0.04}$	205.6 ± 0.3	1.54 ± 0.04	2.41 ± 0.06
1750	4926	6.00 ± 0.75	7.00	$0.15^{+0.47}_{-0.05}$	279.1 ± 1.6	3.41 ± 0.50	5.33 ± 0.79
1990	IC 843	10.00 ± 1.00	10.00	$0.01^{+0.01}_{-0.01}$	281.3 ± 1.1	3.03 ± 0.30	4.74 ± 0.47
2417	4908	8.00 ± 0.75	8.50	$0.05^{+0.20}_{-0.04}$	211.0 ± 1.7	3.78 ± 0.43	5.91 ± 0.67
2440	IC 4045	6.50 ± 0.50	7.00	$0.07^{+0.02}_{-0.02}$	225.9 ± 0.9	3.46 ± 0.27	5.41 ± 0.42
3414	4871	4.00 ± 0.62	6.00	$0.46^{+0.06}_{-0.27}$	169.6 ± 1.3	3.20 ± 0.29	4.99 ± 0.45
3510	4869	5.50 ± 0.50	6.00	$0.09^{+0.18}_{-0.05}$	177.7 ± 1.7	3.49 ± 0.65	5.45 ± 1.02
3792	4860	8.00 ± 1.00	9.00	$0.13^{+0.24}_{-0.05}$	284.0 ± 1.9	4.27 ± 0.31	6.66 ± 0.48
4822	4841A	5.50 ± 1.00	6.50	$0.51^{+0.14}_{-0.27}$	272.1 ± 2.7	3.24 ± 0.33	5.07 ± 0.52
4928	4839	8.50 ± 2.00	10.00	$0.32^{+0.35}_{-0.21}$	314.8 ± 2.9	3.34 ± 0.46	5.22 ± 0.72
5279	4827	6.50 ± 0.50	7.00	$0.10^{+0.21}_{-0.07}$	244.1 ± 1.2	3.16 ± 0.45	4.93 ± 0.71
5568	4816	6.00 ± 1.00	7.00	$0.53^{+0.15}_{-0.25}$	233.4 ± 1.7	3.91 ± 0.33	6.11 ± 0.52
5975	4807	3.00 ± 0.50	4.00	$0.29^{+0.05}_{-0.01}$	195.9 ± 0.8	3.07 ± 0.24	4.80 ± 0.37

We probed two dark matter descriptions. First, logarithmic haloes with a constant-density core of size $r_{\rm h}$ and, secondly, NFW haloes (Navarro, Frenk & White 1996). The latter provide good fits to cosmological N-body simulations and have a central logarithmic slope of -1. Neither of the two profiles includes the baryonic halo contraction explicitly (cf. the discussion in Section 5.2). Coma galaxies are in most cases better fit with logarithmic haloes, but the significance over NFW halo profiles is marginal. The steeper central slope of NFW haloes implies a higher central dark matter density. However, even in cases where NFW haloes fit better, the innermost galaxy regions are still dominated by the mass component that follows the light (for details see Thomas et al. 2007b). The assumptions about the halo-density profile have therefore little influence on the best-fitting stellar mass-to-light ratio $\Upsilon_{*,\rm dyn}$ (typically, $\Upsilon_{*,\rm dyn}$ from logarithmic or NFW haloes differs by no more than $\Delta\Upsilon_{*,\rm dyn} \approx 0.5$; see also Section 4.2).

The gravitational potential of the galaxies is assumed to be axisymmetric. Contrasting other methods like using Jeans equations, the Schwarzschild technique allows the exploration of all possible orbit configurations. The Coma sample is unique in being the only larger sample of axisymmetric dynamical models including dark matter. Previous modelling attempts either assumed spherical symmetry (Gerhard et al. 2001) or did not include dark matter explicitly (Cappellari et al. 2006).

2.2 Stellar population models

Stellar ages, metallicities, [α/Fe] ratios and R-band stellar mass-to-light ratios are determined by fitting the single stellar population models of Maraston (1998, 2005) with the α-element overabundance of Thomas, Maraston & Bender (2003) to the Lick indices Hβ, $\langle$Fe$\rangle$, [MgFe] and Mg b. Two IMFs are considered. First, the Salpeter IMF ($\Upsilon_{\rm Salp}$, with the mass limits of 0.1 and 100 $\rm M_\odot$) and, secondly, the Kroupa IMF ($\Upsilon_{\rm Krou}$, with the same mass limits, but a shallower slope for stars below 0.5 $\rm M_\odot$). The Salpeter IMF implies more low-mass stars and a higher mass-to-light ratio. In the R band, the scaling between the two cases is $\Upsilon_{\rm Salp} \approx 1.56\Upsilon_{\rm Krou}$ (Salpeter 1955; Kroupa 2001). When the IMF does not need to be specified, we will refer to stellar population mass-to-light ratios as $\Upsilon_{\rm ssp}$.

Stellar population properties are calculated at each radius with observations. Salpeter R-band mass-to-light ratios are shown in Fig. 1. The light-weighted averages within $r_{\rm eff}$ are indicated by the dashed lines and form the basis for the remainder of this paper (Table 1). For some galaxies, there are systematic differences between the two sides of a slit which are slightly larger than the statistical errors (e.g. along the major-axis of GMP0144). These systematic uncertainties are not included in the errors quoted in Table 1. Irrespective of the metallicity gradients present in early-type galaxies (Mehlert et al.

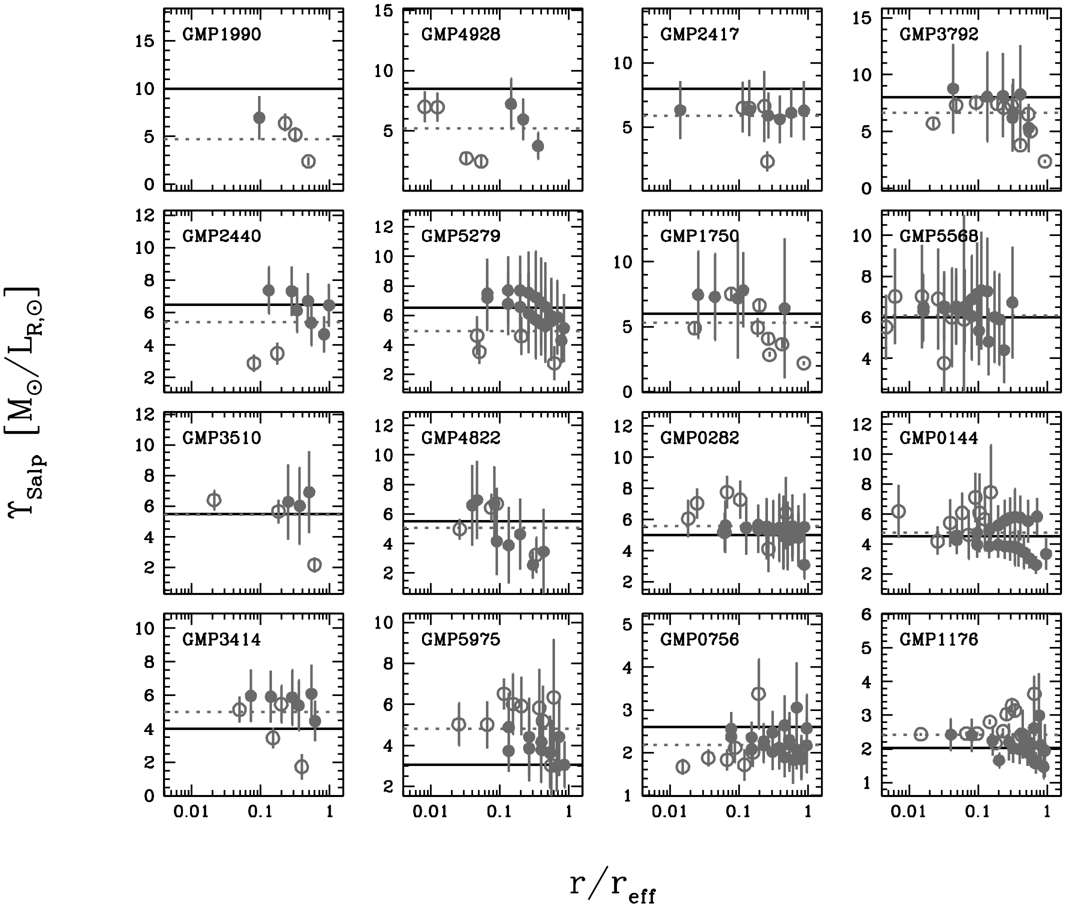

Figure 1. Stellar population mass-to-light ratios, $\Upsilon_{\rm Salp}$ (Salpeter IMF), as function of the radius along the major-axis (filled circles) and minor-axis (open circles). Note that for some galaxies there are systematic differences between the two sides of a slit which are slightly larger than the statistical errors (e.g. along the major-axis of GMP0144). The dotted line in each panel is the light-weighted average of $\Upsilon_{\rm Salp}$ within $r < r_{\rm eff}$, the solid line corresponds to the stellar mass-to-light ratio, $\Upsilon_{*,\rm dyn}$, from dynamical models. From the top left-hand panel to bottom right-hand panel galaxies are plotted in the order of decreasing $\Upsilon_{*,\rm dyn}$.

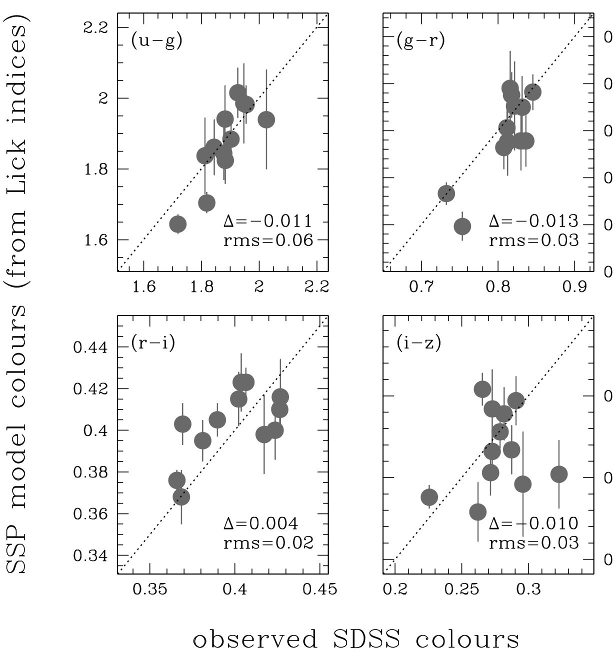

Figure 2. Observed versus predicted colours for the subsample of Coma galaxies with SDSS photometry. Colours as indicated in each panel. Model predictions are plotted along the vertical axis and SDSS observations are plotted horizontally. All axes are in magnitudes. The mean colour difference, Δ, and rms scatter between models and observations (in magnitudes) is quoted in each panel.

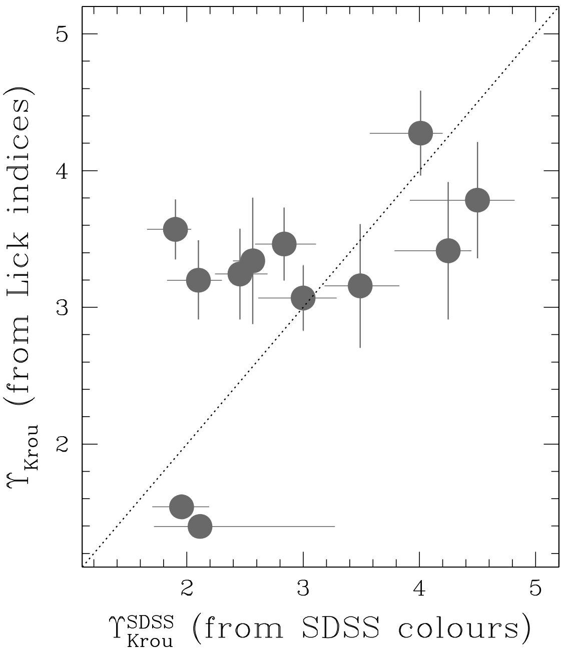

Figure 3. Stellar population $\Upsilon_{\rm Krou}$ (Kroupa IMF) from SDSS colours (*x*-axis; cf. Grillo & Gobat 2010) and from Lick indices (*y*-axis; cf. Table 1).

2003), mass-to-light ratio gradients in the *R* band are generally small for the Coma galaxies (cf. Fig. 1). The results presented here do not depend significantly on the averaging radius. Its choice is driven by the most massive sample objects. Their spectroscopic data reach only out to $r_{\rm obs,max} \approx r_{\rm eff}$ and, for the purpose of homogeneity, we restrict the averaging in other galaxies to the same radius, even if the data extend farther out.

For a subsample of the Coma galaxies studied here, the multiband photometry from the Sloan Digital Sky Survey (SDSS; York et al. 2000) is available. Fig. 2 compares observed SDSS colours with the predictions of our best-fitting single stellar population (SSP) models. We have applied the same colour corrections to the models as discussed in Saglia et al. (2010) plus an additional $i - z = -0.05$ (Maraston, private communication), to take into account the recent improvements in the calibration of the Maraston SSP models (Maraston et al. 2009). The vertical error bars indicate the 68 per cent confidence region derived from the observational errors. Model colours are averaged inside $r_{\rm eff}$. They fit well to the SDSS colours with average differences $\lesssim$0.01 mag.

Grillo & Gobat (2010) used observed SDSS colours to derive photometric stellar population parameters for some of our Coma galaxies. In contrast to the analysis presented here, they (1) assume a solar metallicity for all galaxies (but see the middle panel of Fig. 11 shown later); (2) allow for an extended star formation history; and (3) use the Maraston (2005) models without colour corrections. In Fig. 3, we plot their photometric $\Upsilon^{\rm SDSS}_{\rm Krou}$ (scaled to the Kroupa IMF) against our $\Upsilon_{\rm Krou}$. On average, both approaches yield consistent results ($\langle \Upsilon_{\rm Krou}/\Upsilon^{\rm SDSS}_{\rm Krou}\rangle = 1.11$), though the rms scatter between them (±0.35) is large.

3 PROJECTED MASSES FROM DYNAMICS AND LENSING

As it has been stated in Section 1, the dynamical models rely on the assumption of axial symmetry and steady-state dynamics. To check how accurately these assumptions are fulfilled in real galaxies, we first compare our dynamical models against gravitational lensing results. The latter constrain the total projected mass inside a cylinder delimited by the Einstein radius, $r_{\rm Ein}$, of the lens and are less affected by symmetry assumptions (Kochanek 1991).

3.1 Lens selection

The Einstein radius of a gravitational lens results from two independent properties of a lensing configuration. First, from the physical deflection angle that the lensing galaxy gives rise to according to its gravity. It depends only on the mass distribution of the foreground galaxy. Secondly, from projection factors that depend on the distances of the foreground lens and the background source. For the Coma galaxies, we only know their mass distributions, but they are not part of real lenses. To compare them with observed gravitational lenses, we need to define an appropriate lensing configuration for each Coma galaxy. Here we do this implicitly by seeking for lensing galaxies that accidentally happen to fall on a linear relation $r_{\rm Ein}(\sigma_{\rm eff})$ between the Einstein radius and the effective velocity dispersion. Defining a fiducial Einstein radius for each Coma galaxy according to the same $r_{\rm Ein}(\sigma_{\rm eff})$ then ensures that there is at least a subsample of real lenses with similar lens configurations at a given $\sigma_{\rm eff}$. The Coma galaxies can be compared to the lenses in such a subsample, but not to the rest of the lensing galaxies. The form of the selection function is arbitrary; any other function would serve equally well. We choose a linear relation for simplicity.

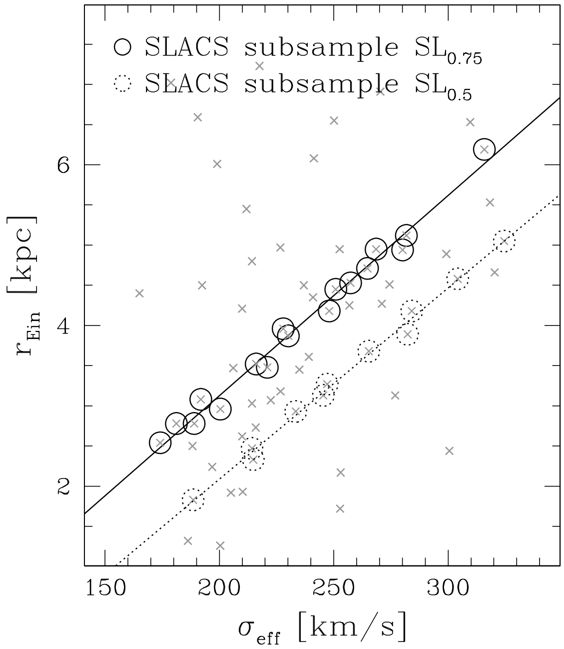

Figure 4. Einstein radii, $r_{\rm Ein}$, and effective velocity dispersions, $\sigma_{\rm eff}$, of SLACS galaxies from Auger et al. (2009) are shown by the crosses. The dotted open circles highlight lenses that follow equation (4), shown by the dotted line, and form subsample $SL_{0.5}$; the solid open circles are for subsample $SL_{0.75}$ (i.e. galaxies that follow equation 5, shown by the solid line).

Fig. 4 shows the observed Einstein radii, $r_{\rm Ein}$, of SLACS lenses from Auger et al. (2009) against their velocity dispersions.[1] The large circles show two different subsamples of lenses constructed as outlined above. The lenses are selected to deviate by less than 0.2 kpc from two arbitrary linear selection functions, $r_{\rm Ein}(\sigma_{\rm eff}) = 0.025\sigma_{\rm eff} - 3.0$ and $r_{\rm Ein}(\sigma_{\rm eff}) = 0.025\sigma_{\rm eff} - 1.9$. After having selected the lenses, we fit a straight line to each subsample in order to determine the actual best-fitting $r_{\rm Ein}(\sigma_{\rm eff})$ that is used to define fiducial Einstein radii for Coma galaxies. The fitted relations differ only slightly from the original selection functions. For subsample $SL_{0.5}$ (dotted line), we get

$$\frac{r_{\rm Ein}}{\rm kpc} = 0.0238 \times \frac{\sigma_{\rm eff}}{\rm km\,s^{-1}} - 2.6709 \qquad (4)$$

and for subsample $SL_{0.75}$ (solid line), we have

$$\frac{r_{\rm Ein}}{\rm kpc} = 0.0249 \times \frac{\sigma_{\rm eff}}{\rm km\,s^{-1}} - 1.8564. \qquad (5)$$

The two subsamples are constructed as a compromise between (1) ending up with a sizeable number of galaxies in each subsample and (2) yielding sufficiently different subsamples to allow for a comparison between Coma and lensing galaxies at different physical scales. For subsample $SL_{0.5}$, we get an average $\langle r_{\rm Ein}/r_{\rm eff}\rangle \approx 0.5$ (11 lenses), while for subsample $SL_{0.75}$, it is $\langle r_{\rm Ein}/r_{\rm eff}\rangle \approx 0.75$ (17 lenses).

3.2 The total mass

The large symbols in Fig. 5 show projected, integrated masses of Coma galaxies and SLACS lenses as a function of the galaxy velocity dispersion $\sigma_{\rm eff}$. Coma masses are calculated from the integral

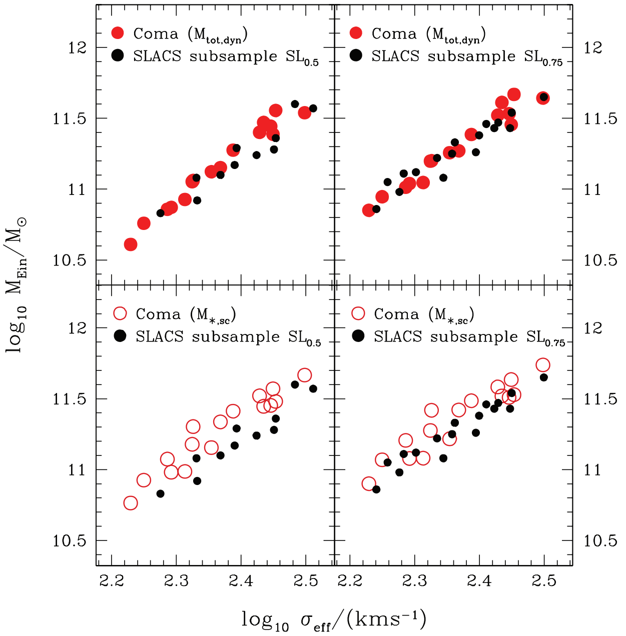

Figure 5. The projected total (luminous+dark) mass, $M_{\rm Ein}$, within a fiducial Einstein radius $r_{\rm Ein}$. Coma galaxies are indicated by the large symbols. Top row: two-component models with dark matter haloes ($\rho = \Upsilon_{*,\rm dyn} \times \nu + \rho_{\rm DM,dyn}$ in equation 6). Bottom row: dynamical mass under the assumption that mass follows light ($\rho = \Upsilon_{*,\rm sc} \times \nu$). Small circles: total projected masses of SLACS galaxies (Auger et al. 2009). In the left-hand panels, we compare Coma galaxies with SLACS subsample $SL_{0.5}$ using fiducial Einstein radii calculated via equation (4). In the right-hand panels, we compare to subsample $SL_{0.75}$ (using equation 5). Masses are plotted against the average velocity dispersion, $\sigma_{\rm eff}$, inside $r_{\rm eff}$.

$$M_{\rm Ein} \equiv \int_{-10r_{\rm eff}}^{10r_{\rm eff}} {\rm d}z \int_0^{2\pi} {\rm d}\varphi \int_0^{r_{\rm Ein}(\sigma_{\rm eff})} \rho\, r\, {\rm d}r, \qquad (6)$$

where (r, φ) are polar coordinates on the sky and z is the direction of the line of sight. Formally, the integral in equation (6) should be calculated over $-\infty \le z \le +\infty$, but we limited it over $-10r_{\rm eff} \le z \le +10r_{\rm eff}$. For an isothermal sphere, this cut-off results in a negligible underestimation of the integral ($\approx$4 per cent). Coma galaxy velocity dispersions, $\sigma_{\rm eff}$, are measured by (1) reconstructing the line-of-sight velocity distributions (LOSVDs) from the kinematic moments; (2) co-adding all LOSVDs inside $r_{\rm eff}$, each weighted by its projected light; and (3) fitting a Gaussian to the resulting LOSVD. They are listed in Table 1. Because of their higher signal-to-noise ratio, only the major-axis data have been considered. The upper integration limit, $r_{\rm Ein}(\sigma_{\rm eff})$, in equation (6) refers to equation (4) for the comparison with SLACS subsample $SL_{0.5}$ and to equation (5) for the comparison with subsample $SL_{0.75}$. In Fig. 5, we only show those SLACS lenses that belong to either subsample $SL_{0.5}$ (left-hand panels) or subsample $SL_{0.75}$ (right-hand panels).

The top row is for the total cylindrical mass of our standard two-component models with dark matter haloes (i.e. with the best-fitting density $\rho = \Upsilon_{*,\rm dyn} \times \nu + \rho_{\rm DM,dyn}$ in equation 6). The good agreement with the lensing results is reassuring (the average mass offset is 0.05 dex for subsample $SL_{0.5}$ and 0.02 dex for subsample $SL_{0.75}$). It implies that the two completely independent methods yield consistent results. Moreover, the scatter in the dynamical masses is not larger than in the lensing masses. Consequently, strong deviations from axisymmetry are unlikely in the Coma galaxies. As shown in

---

[1] Note that for Fig. 4 we have used the correction of Cappellari et al. (2006) to transform the measured SDSS aperture dispersions into $\sigma_{\rm eff}$.

Thomas et al. (2007a), strong triaxiality, if not accounted for in the models, can bias dynamical masses by a factor of up to 2, depending on the viewing angle. Assuming random viewing angles, strongly triaxial mass distributions would therefore likely cause a significant scatter in the dynamical masses, which is, however, not observed (but see van de Ven, Mandelbaum & Keeton 2009).

The bottom row of Fig. 5 is for projected masses of self-consistent dynamical models in which all the mass is assumed to follow the light (i.e. $\rho = \Upsilon_{*,\mathrm{sc}} \times \nu$). These models are not consistent with the lensing masses. The discrepancy is larger for SLACS subsample $\mathrm{SL}_{0.5}$ than for subsample $\mathrm{SL}_{0.75}$ because the smaller Einstein radii of subsample $\mathrm{SL}_{0.5}$ emphasize the central regions in the comparison. As it has been shown earlier (e.g. Gerhard et al. 2001; Thomas et al. 2007b), the mass distribution in early-type galaxies follows the light in the inner regions ($\rho_{\mathrm{in}} \approx \Upsilon_{*,\mathrm{dyn}} \times \nu_{\mathrm{in}}$), but has an additional component in the outer parts ($\rho_{\mathrm{out}} \approx \Upsilon_{*,\mathrm{dyn}} \times \nu_{\mathrm{out}} + \rho_{\mathrm{DM}}$). Then, assuming that all the mass follows the light requires $\Upsilon_{*,\mathrm{sc}} > \Upsilon_{*,\mathrm{dyn}}$ to include the outer dark matter ($\Upsilon_{*,\mathrm{sc}} \times \nu_{\mathrm{out}} \approx \rho_{\mathrm{out}} \approx \Upsilon_{*,\mathrm{dyn}} \times \nu_{\mathrm{out}} + \rho_{\mathrm{DM}}$). However, the central regions become proportionally more massive, too, such that $\Upsilon_{*,\mathrm{sc}} \times \nu_{\mathrm{in}} > \Upsilon_{*,\mathrm{dyn}} \times \nu_{\mathrm{in}} \approx \rho_{\mathrm{in}}$. This explains why the offset in the lower left-hand panel of Fig. 5 is larger than in the lower right-hand one.

3.3 Stellar population masses

In Fig. 6, we show projected *stellar* masses (i.e. using $\rho = \Upsilon_{\mathrm{Salp}} \times \nu$ and $\rho = \Upsilon_{\mathrm{Krou}} \times \nu$ in equation 6). The open dots in these panels represent the projected *stellar* masses for either the Salpeter IMF (top row) or the Kroupa IMF (bottom row). Kroupa stellar masses are always below lensing masses. The mass difference between the lenses and the Kroupa masses increases from subsample $\mathrm{SL}_{0.5}$ to subsample $\mathrm{SL}_{0.75}$ for the same reason discussed at the end of Section 3.2. It could be due to dark matter. Salpeter stellar masses are likewise consistent with the lensing results. In low-dispersion galaxies, the IMF cannot be much steeper than Salpeter as otherwise the implied stellar masses would exceed the total observed lens masses. In high-dispersion galaxies, the Salpeter stellar masses are, however, not enough to explain the total lensing masses. Then, if all the lensing mass were stellar, then the IMF would have to change with the galaxy velocity dispersion and in massive early types, the stellar mass per stellar light would have to be larger than for a Salpeter IMF (or any equivalent top-heavy IMF). If the IMF is constant, then the top left-hand panel of Fig. 6 provides direct evidence for the presence of dark matter in high-dispersion early-type galaxies.

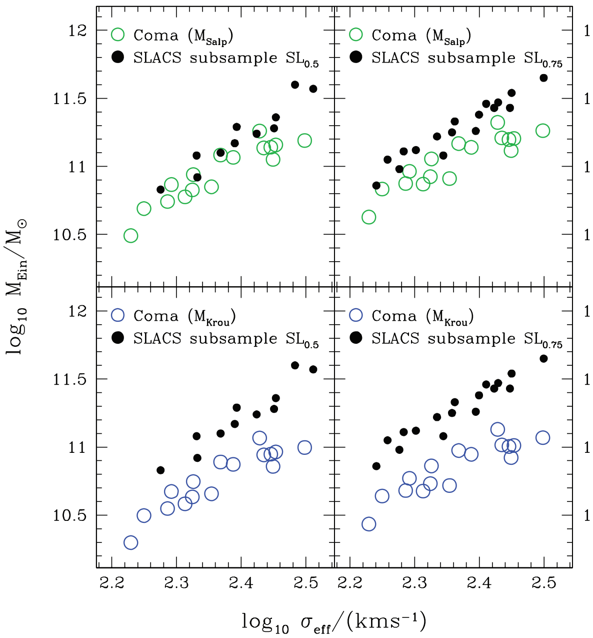

Figure 6. As in Fig. 5, but for stellar population masses. Top row: Salpeter IMF ($\rho = \Upsilon_{\mathrm{Salp}} \times \nu$). Bottom row: Kroupa IMF ($\rho = \Upsilon_{\mathrm{Krou}} \times \nu$).

3.4 Luminous and dark matter separated

In our standard two-component models that take into account the detailed, radially resolved stellar kinematics, the large projected masses of high-dispersion galaxies do not entirely originate from luminous mass. This is shown in the top panel of Fig. 7 (projected dark matter fractions inside the Einstein radius). Note that here we compare to the results of Koopmans et al. (2006), who provided a combined lensing and dynamics analysis of the first SLACS galaxies. We applied a similar lens selection as described in Section 3.1 (using $r_{\mathrm{Ein}} = 0.032\,44 \times \sigma_{\mathrm{eff}} - 4.6324$). Our dynamically derived dark matter fractions are in good agreement with those from

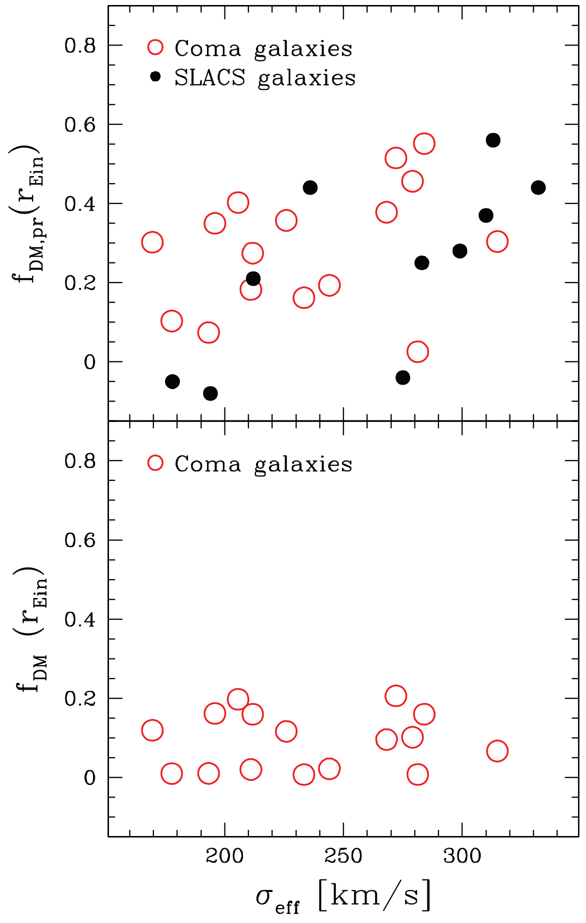

Figure 7. Dark matter fractions inside the Einstein radius. Top panel: projected dark matter fraction. Bottom panel: deprojected dark matter fraction. Red/open circles: Coma galaxies of this work; dark/filled circles in the top panel: SLACS galaxies from Koopmans et al. (2006). Coma galaxy dark matter fractions are plotted against the velocity dispersion, σ_{eff}, inside r_{eff}. SLACS galaxies are plotted against the measured velocity dispersion inside the SDSS aperture.

Koopmans et al. (2006). As already stated above, they increase with $\sigma_{\rm eff}$. For comparison, we have also plotted the corresponding deprojected dark matter fractions (cf. equation 3) inside the same three-dimensional radius $r_{\rm Ein}(\sigma_{\rm eff})$ in the bottom panel of Fig. 7. They are generally lower and do not vary with $\sigma_{\rm eff}$. Projection effects therefore contribute to the trends in Figs 5–7. To get a better understanding about the stellar IMF and dark matter distribution, it is necessary to analyse the intrinsic three-dimensional properties of the galaxies. This will be done in Sections 4 and 5.

4 DYNAMICAL LUMINOUS MASS VERSUS STELLAR POPULATION MASS

Fig. 8 shows dynamical and stellar population mass-to-light ratios versus $\sigma_{\rm eff}$. The dynamical ratios, $\Upsilon_{*,\rm dyn}$, exhibit a broad distribution ranging from $\Upsilon_{*,\rm dyn} \approx 2$ to ≈ 10. In contrast, for the majority of Coma galaxies, the stellar population $\Upsilon_{\rm ssp}$ are almost constant with $\Upsilon_{\rm Salp} \approx 5$–6 for the Salpeter IMF and $\Upsilon_{\rm Krou} \approx 3$–4 for the Kroupa IMF. In addition, while the dynamical $\Upsilon_{*,\rm dyn}$ clearly increase with the galaxy velocity dispersion, there is no similar correlation between $\sigma_{\rm eff}$ and the stellar population $\Upsilon_{\rm ssp}$.

There are two galaxies (GMP0756 and GMP1176) with distinctly lower stellar mass-to-light ratios than in the rest of the sample. As Fig. 9 shows, these two galaxies have overall young stellar populations (as it often happens in similar low dispersion galaxies, e.g., Thomas et al. 2005b). In general, one can read off from Figs 8 and 9 that the dynamical $\Upsilon_{*,\rm dyn}$ depend on $\sigma_{\rm eff}$ but not primarily on the stellar population age, while $\Upsilon_{\rm ssp}$ mostly reflect stellar ages and do not show any dependency on $\sigma_{\rm eff}$.

4.1 Variation in the stellar IMF?

Since dynamical and stellar population masses scale differently with the galaxy velocity dispersion (cf. Fig. 8), the ratio $\Upsilon_{*,\rm dyn}/\Upsilon_{\rm ssp}$ has to vary with the galaxy $\sigma_{\rm eff}$ (for any fixed IMF). This is explicitly shown by the large/red symbols in Fig. 10. In addition to our results, the figure also combines work from other groups.

The pentagons represent the stellar population analysis of a subsample of our Coma galaxies by Grillo & Gobat (2010) (cf. Section 2.2). The pentagons differ from the large filled symbols only in terms of $\Upsilon_{\rm Krou}$. The velocity dispersions and dynamical $\Upsilon_{*,\rm dyn}$ are the same.

Triangles are for the SAURON survey (Cappellari et al. 2006). In terms of both, the stellar population analysis (based on spectral absorption line indices) and the dynamical modelling (orbit-based), they can be most directly compared to the Coma galaxies of this work. Note, however, that Cappellari et al. (2006) measured only the sum of luminous and dark masses, assuming the latter to contribute only a small amount of mass in the central galaxy regions

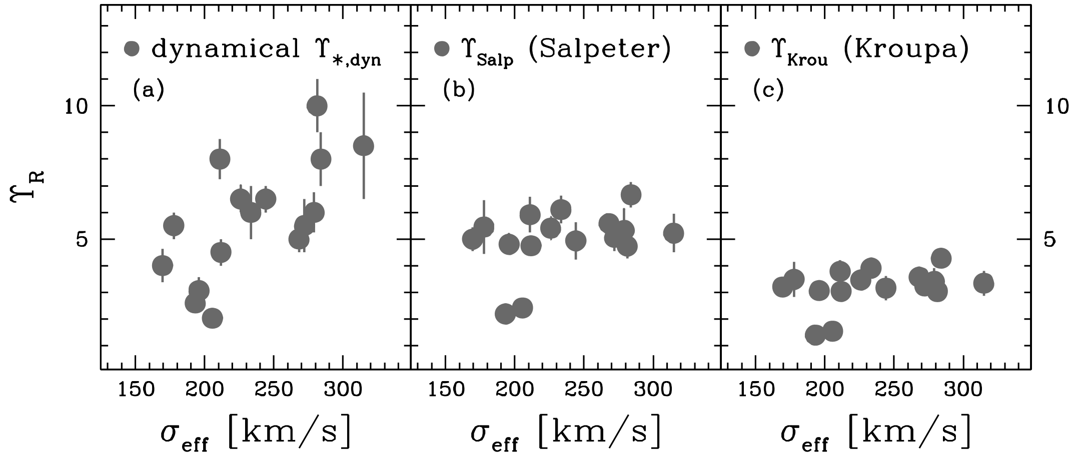

Figure 8. Stellar mass-to-light ratios (*R* band) against average velocity dispersion, $\sigma_{\rm eff}$, inside $r_{\rm eff}$. From the left- to right-hand side: (a) dynamical $\Upsilon_{*,\rm dyn}$; (b) stellar population $\Upsilon_{\rm Salp}$ for the Salpeter IMF; and (c) stellar population $\Upsilon_{\rm Krou}$ for the Kroupa IMF.

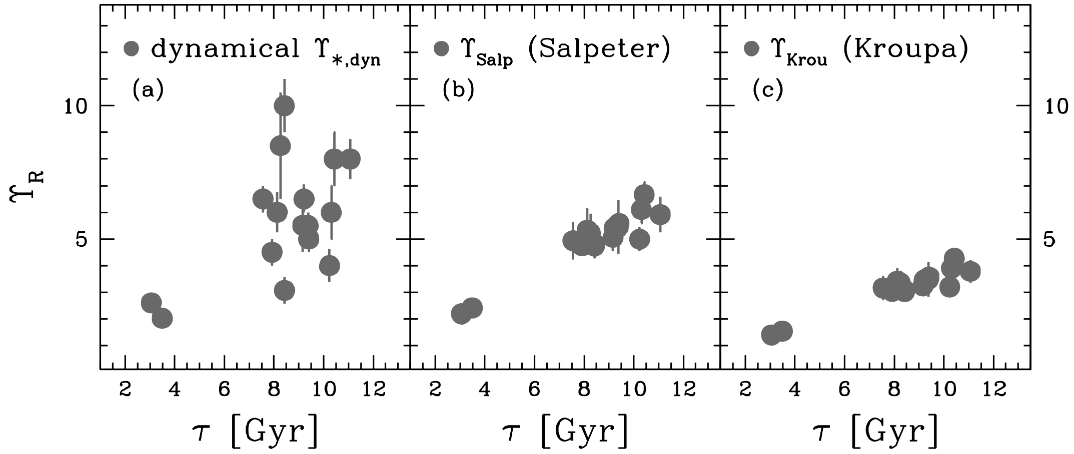

Figure 9. As in Fig. 8, but stellar mass-to-light ratios are plotted against the stellar population age τ.

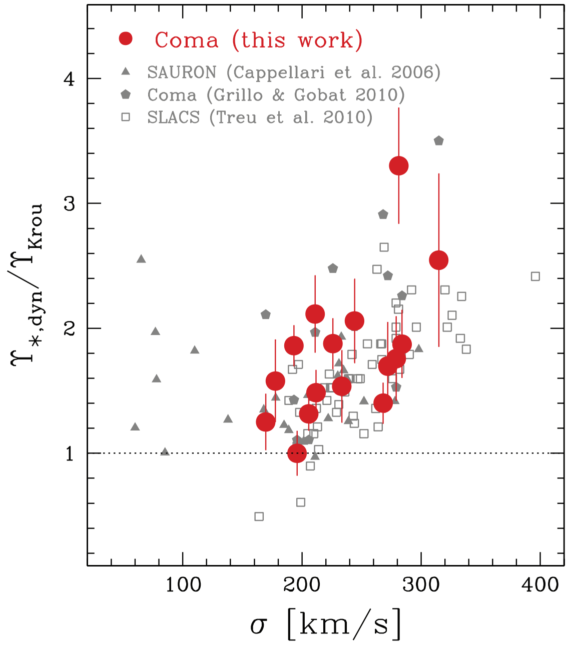

Figure 10. Ratio $\Upsilon_{*,\mathrm{dyn}}/\Upsilon_{\mathrm{Krou}}$ versus velocity dispersion σ. Large, filled circles: spectroscopic Υ_{Krou} and orbit-based dynamical models accounting for dark matter (this work); filled triangles: spectroscopic Υ_{Krou} and orbit-based dynamical models, neglecting dark matter (Cappellari et al. 2006); filled pentagons: photometric Υ_{Krou} (Grillo & Gobat 2010) and orbit-based dynamical models accounting for dark matter; and open squares: photometric Υ_{Krou} and combined lensing + dynamics models (Treu et al. 2010). For all but the SLACS galaxies, the average velocity dispersion, σ_{eff}, inside r_{eff} is plotted. The SLACS dispersions are the average over the spectroscopic aperture of the SDSS.

observed with SAURON ($r_{\mathrm{obs,max}} \lesssim r_{\mathrm{eff}}$). Adopting equivalent modelling assumptions for the Coma galaxies yields mass-to-light ratios typically 10–20 per cent higher than compared with stellar $\Upsilon_{*,\mathrm{dyn}}$ from models where dark matter is accounted for explicitly (cf. Table 1). The overall distributions of $\Upsilon_{*,\mathrm{dyn}}/\Upsilon_{\mathrm{Krou}}$ are nevertheless similar in both samples.

Finally, Fig. 10 also includes SLACS galaxies, analysed with a combined dynamics and lensing approach (Treu et al. 2010). For these galaxies, the ratio of the total versus the stellar mass (the latter derived from broad-band colours) inside the Einstein radius (typically of the order of $r_{\mathrm{eff}}/2$) is plotted along the y-axis.

In all the samples included in Fig. 10, dynamical (or lensing) stellar masses systematically exceed the required masses for a Kroupa IMF. Above $\sigma_{\mathrm{eff}} \gtrsim 150\,\mathrm{km\,s^{-1}}$, the ratio $\Upsilon_{*,\mathrm{dyn}}/\Upsilon_{\mathrm{Krou}}$ tends to increase with the velocity dispersion. For lower mass galaxies, the ratio becomes uncertain due to the more frequent presence of multiple stellar populations (e.g. Cappellari et al. 2006). Moreover, for low-mass galaxies, the assumption that all the mass follows the light is in conflict with gravitational lensing masses (cf. Section 3).

If the increase in $\Upsilon_{*,\mathrm{dyn}}/\Upsilon_{\mathrm{Krou}}$ with σ_{eff} were a pure stellar population effect, then we would have to assume that the IMF is not universal. Interpreted in this way, Fig. 10 would imply the IMF in high-dispersion galaxies to produce either more low-mass stars than the Kroupa IMF (i.e. being Salpeter like) or more stellar remnants (i.e. being top heavy). A higher fraction of low-mass stars would reduce the number of Type II supernovae (SNe II) (per stellar mass) and would lead to an overall lower metallicity. Thus, if the IMF changes from Kroupa towards Salpeter, then the increase in $\Upsilon_{*,\mathrm{dyn}}/\Upsilon_{\mathrm{Krou}}$ would be expected to come along with a decrease in metallicity [Z/H]. Instead, a top-heavy IMF enhances the importance of SNe II over SNe Ia. Accordingly, if the IMF changes from Kroupa towards being top heavy, then one would expect higher [α/Fe] in galaxies with higher $\Upsilon_{*,\mathrm{dyn}}/\Upsilon_{\mathrm{Krou}}$ (Thomas, Greggio & Bender 1999; Graves & Faber 2010).

Fig. 11 shows $\Upsilon_{*,\mathrm{dyn}}/\Upsilon_{\mathrm{Krou}}$ against the stellar population age τ, metallicity [Z/H] and [α/Fe] ratio. There is no correlation with any stellar population parameter. Note, however, that stellar metallicities and [α/Fe] ratios depend not only on the stellar IMF, but also on the duration of the star formation episode(s), the depth of the galaxy potential well and on evolutionary processes related to the cluster environment. In this respect, the lack of evidence for an IMF change cannot be taken as a proof for a constant IMF. Alternatives to IMF variations are discussed in Sections 4.4 and 5.2.

4.2 The shape of the stellar IMF

A direct comparison between dynamical and stellar population mass-to-light ratios is provided in Fig. 12. As already clear from the different scalings of $\Upsilon_{*,\mathrm{dyn}}$, on the one hand, and Υ_{ssp}, on the other hand (cf. Figs 8 and 9), neither the Kroupa IMF nor the Salpeter IMF yields a close match between $\Upsilon_{*,\mathrm{dyn}}$ and Υ_{ssp}.

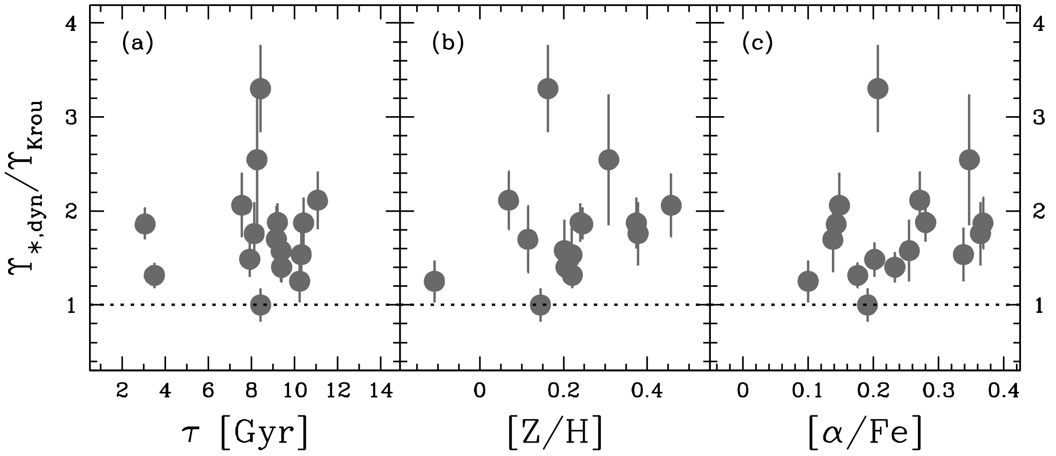

Figure 11. Ratio $\Upsilon_{*,\mathrm{dyn}}/\Upsilon_{\mathrm{Krou}}$ against the stellar population age τ (panel a), metallicity [Z/H] (panel b) and abundance ratio [α/Fe] (panel c).

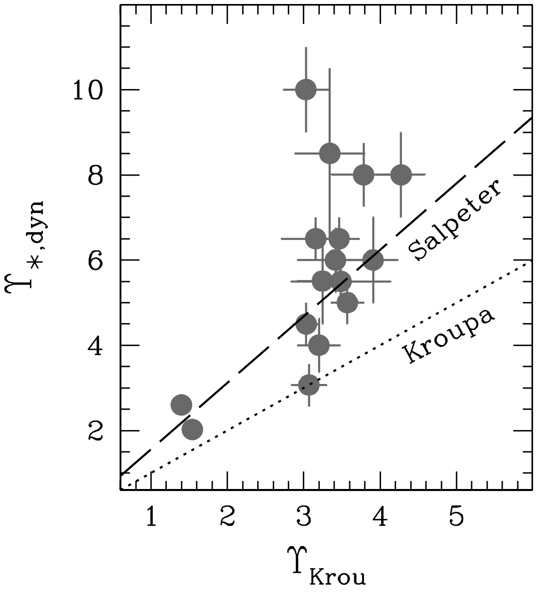

Figure 12. Dynamical $\Upsilon_{*,\mathrm{dyn}}$ versus stellar population mass-to-light ratio Υ_{Krou}. The dotted line shows the one-to-one relation for the Kroupa IMF. Since $\Upsilon_{\mathrm{Salp}} = 1.6 \times \Upsilon_{\mathrm{Krou}}$, the corresponding one-to-one relation for the Salpeter IMF occurs at larger $\Upsilon_{*,\mathrm{dyn}}$ (dashed line).

Above the dotted line in Fig. 12, the luminous dynamical mass is larger than the stellar mass required for the Kroupa IMF, while below the line, the dynamical $\Upsilon_{*,\mathrm{dyn}}$ is formally insufficient for the Kroupa IMF. For the Salpeter IMF, the corresponding limit is shifted towards $\Upsilon_{*,\mathrm{dyn}}$ which are a factor of 1.6 higher (dashed line). Accordingly, all Coma galaxies are compatible with a Kroupa IMF. The majority of the galaxies are also consistent with a Salpeter IMF, but there is at least one galaxy for which the dynamical $\Upsilon_{*,\mathrm{dyn}}$ is significantly lower than Υ_{Salp} (at about the 3σ level; GMP5975). Concerning the total sample, however, the Salpeter IMF fits the dynamical masses better than the Kroupa IMF. The corresponding sample averages are $\langle\Upsilon_{*,\mathrm{dyn}}/\Upsilon_{\mathrm{Salp}}\rangle = 1.15$ for the Salpeter IMF (with an rms scatter of 0.35) and $\langle\Upsilon_{*,\mathrm{dyn}}/\Upsilon_{\mathrm{Krou}}\rangle = 1.8$ for the Kroupa IMF.

These conclusions also hold for other galaxy samples. Since $\Upsilon_{\mathrm{Salp}} \approx 1.6 \times \Upsilon_{\mathrm{Krou}}$, the one-to-one line for the Salpeter IMF in Fig. 10 would occur at $\Upsilon_{*,\mathrm{dyn}}/\Upsilon_{\mathrm{ssp}} \approx 1.6$. Then, the Salpeter IMF provides *on average* a better match with dynamical/lensing masses. In line with this, recent near-infrared spectroscopic observations point towards a bottom-heavy IMF in massive early-type galaxies as well (van Dokkum & Conroy 2010, 2011). However, our dynamical models as well as previous lensing studies (Ferreras et al. 2010; Treu et al. 2010) indicate that around $\sigma_{\mathrm{eff}} \lesssim 200\,\mathrm{km\,s^{-1}}$ the Salpeter stellar masses exceed the observed dynamical and/or lensing limits. This rules out a Salpeter IMF for low-mass galaxies.

The results for the Coma galaxies are largely independent of the parametrization chosen for the dark matter haloes. Fits with logarithmic haloes alone yield $\langle\Upsilon^{\mathrm{LOG}}_{*,\mathrm{dyn}}/\Upsilon_{\mathrm{Salp}}\rangle = 1.16$, while NFW haloes result in $\langle\Upsilon^{\mathrm{NFW}}_{*,\mathrm{dyn}}/\Upsilon_{\mathrm{Salp}}\rangle = 1.06$. Both are consistent within the rms scatter (about $\approx$0.32).

4.3 Uncertainties in population Υ_{ssp}

Gas emission can refill the Hβ line and lead to an overestimate of stellar population ages and then of Υ_{ssp}. A young stellar population (dominating in terms of light, but not in terms of mass) can likewise bias stellar ages and Υ_{ssp}, yet towards too low values. In any case, $\Upsilon_{*,\mathrm{dyn}}/\Upsilon_{\mathrm{ssp}}$ would systematically decrease with the stellar population age. Fig. 11(a) shows, however, that this is not the case in the Coma galaxies, such that a strong bias due to gas emission or young stellar populations is unlikely.

The stellar population parameters of the Coma galaxies are derived from spectral indices and, thus, represent averages along the line of sight. In other words, at a given radius of observation, r_{obs}, the SSP parameters combine the properties of stars with $r > r_{\mathrm{obs}}$. In contrast, dynamical models are most sensitive to the mass distribution inside r_{obs}. Projection effects can therefore introduce a systematic bias between dynamical $\Upsilon_{*,\mathrm{dyn}}$ and stellar population Υ_{ssp} if the stellar population changes with the radius. A monotonic stellar population gradient is enhanced after the projection along the line of sight but diminished in the cumulative mass-to-light ratio constrained by dynamical models (Thomas 2006). More specifically, a radial increase in Υ leads to an underestimation of $\Upsilon_{*,\mathrm{dyn}}/\Upsilon_{\mathrm{ssp}}$ and a radial decrease in Υ leads to an overestimation of $\Upsilon_{*,\mathrm{dyn}}/\Upsilon_{\mathrm{ssp}}$. For a rather steep gradient of $\mathrm{d}\log\Upsilon/\mathrm{d}\log r = \pm0.23$ (a change by a factor of 1.7 per decade in radius), the expected systematic difference between $\Upsilon_{*,\mathrm{dyn}}$ and Υ_{ssp} would amount to $\mp$30 per cent inside r_{eff} (Thomas 2006). The observed gradients in the Coma galaxies are, however, much smaller (cf. Fig. 1). Therefore, systematics due to projection effects seem negligible.

4.4 Uncertainties and interpretation of dynamical $\Upsilon_{*,\mathrm{dyn}}$

The dynamical mass-to-light ratios, $\Upsilon_{*,\mathrm{dyn}}$, could be affected by systematic biases in the modelling process, for example, arising from false symmetry assumptions. As it has been stated in Section 1, the luminous $\Upsilon_{*,\mathrm{dyn}}$ can be biased by a factor of up to 2, if the studied galaxies deviate significantly from the symmetry assumed in our models (Thomas et al. 2007a). However, there is no evidence for the Coma galaxies to be strongly non-axisymmetric. First, they do not show significant isophotal twists as would be indicative for triaxiality. Secondly, as already discussed in Section 3, the good match between dynamical and strong-lensing masses provides further evidence that the obtained dynamical masses are unbiased.

Even if the luminous $\Upsilon_{*,\mathrm{dyn}}$ are accurate, they might not represent the galaxy *stellar* mass in a one-to-one fashion. Ambiguities can come from any non-stellar mass that follows the light and contributes to $\Upsilon_{*,\mathrm{dyn}}$.

Such a mass component could be gas-loss during stellar evolution. It is not included in our Υ_{ssp}, which only encompass the baryonic mass locked in stars or stellar remnants. For a 10-Gyr-old population, the lost gas mass amounts to about 40 per cent of the originally formed stellar mass (e.g. Maraston 2005). Provided that it remains in the galaxies and provided it follows the light distribution, it would contribute to the dynamical mass $\Upsilon_{*,\mathrm{dyn}}$, and the actual baryonic mass in stars and stellar remnants would only be $(f_*\Upsilon_{\mathrm{dyn}}) \times L$ (with $f_* \approx 0.6$). Correcting the dynamical $\Upsilon_{*,\mathrm{dyn}}$ for the stellar mass-loss yields formally a good agreement with the Kroupa IMF: $\langle(f_*\Upsilon_{\mathrm{dyn}})/\Upsilon_{\mathrm{Krou}}\rangle = 1.04 \pm 0.32$.

Theoretical arguments indicate that most of the lost gas is either expelled from the galaxies or recycled into new stars. Only a few per cent of the original stellar mass is expected to remain in hot gas haloes around the galaxies (e.g. Ciotti et al. 1991; David, Forman & Jones 1991). Fittingly, observed gas mass fractions of hot X-ray haloes around massive early-type galaxies are typically less than a per cent of the present stellar mass (e.g. Matsushita 2001), such that the stellar mass-loss is unlikely to explain the excess $\Upsilon_{*,\mathrm{dyn}} > \Upsilon_{\mathrm{Krou}}$.

A possible component of non-baryonic matter that follows the light is discussed below in Section 5.2.

5 DARK MATTER

5.1 Mass that does not follow the light

Fig. 13 shows the spherically averaged three-dimensional density distributions of luminous and dark matter, as well as the sum of both. The sample is subdivided into galaxies with logarithmic halo circular velocities $v_{\rm h} \leq 400\,{\rm km\,s^{-1}}$ and galaxies with $v_{\rm h} > 400\,{\rm km\,s^{-1}}$. The reason is that the latter galaxies have very uniform outer dark and total mass density profiles. The corresponding dark matter fractions (inside $r_{\rm eff}$) scatter around a mean of $\langle f_{\rm DM,dyn}\rangle = 23 \pm 17$ per cent and do not depend on $\sigma_{\rm eff}$. Note that in the central galaxy regions, our models implicitly maximize the mass contribution from the light. Similar maximum-bulge models for lensing galaxies yield dark matter fractions around 25 per cent as well (Barnabè et al. 2009).

Fig. 14 shows the logarithmic slope of the luminosity density and the total mass density in the Coma galaxies. The slope is plotted against the ratio of dark to luminous matter densities at the same radii. In the inner regions, the slope of the total mass density follows the light, since dark matter is negligible ($\rho_{*,\rm dyn} \gg \rho_{\rm DM,dyn}$), and in the outer regions, the total mass density profile is flatter than the light profile. Overall, the total mass density is roughly isothermal: $\rho \sim r^{-2}$. This reflects the nearly-flat circular velocity curves of early-type galaxies (Gerhard et al. 2001; Thomas et al. 2007b). Similar slopes for the total mass distribution have been seen in lensing galaxies (Koopmans et al. 2006; Barnabe et al. 2011). Fig. 14 illustrates that the actual need for a dark matter component in our models comes from the fact that the outer mass distribution does not follow the light in early-type galaxies. The radius where the density of dark matter takes over that of luminous matter is roughly where the slope of the luminosity density falls below $\xi \approx -2.8$ (indicated by the horizontal dotted lines in Fig. 14).

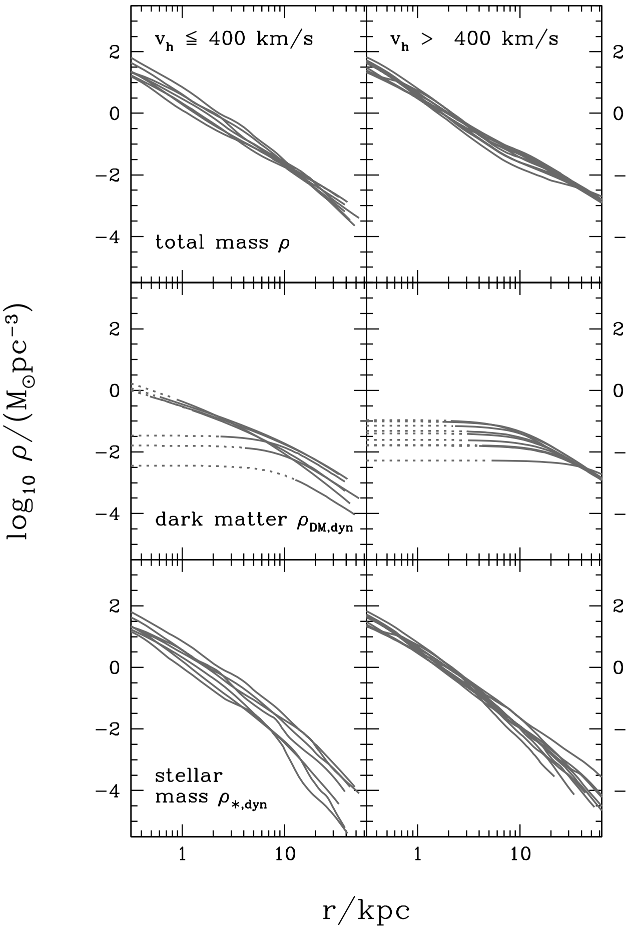

Figure 13. From the top to bottom: total (luminous + dark) three-dimensional mass density, ρ, dark matter density, $\rho_{\rm DM,dyn}$, and luminous mass density, $\rho_{*,\rm dyn}$. All densities are spherically averaged. Left-hand panels: galaxies with less-massive haloes ($v_{\rm h} \leq 400\,{\rm km\,s^{-1}}$); right-hand panels: galaxies with massive haloes ($v_{\rm h} > 400\,{\rm km\,s^{-1}}$). In the middle row, the dotted lines indicate the spatial region where $\rho_{\rm DM,dyn} < \rho_{*,\rm dyn}/10$.

5.2 A component of dark matter that follows the light?

A galaxy might have more dark matter than captured by $\rho_{\rm DM,dyn}$ if some fraction of the halo mass follows the light so closely that it is mapped on to $\Upsilon_{*,\rm dyn}$ rather than $\rho_{\rm DM,dyn}$. In particular, Fig. 14 leaves the possibility open that this could happen in the inner galaxy regions where the slope of the luminosity distribution is $-2 \lesssim \xi \lesssim -1$. If the fraction of dark matter that follows the light is larger in galaxies with higher $\sigma_{\rm eff}$, then this would be a possible explanation for the trend between $\Upsilon_{*,\rm dyn}/\Upsilon_{\rm Krou}$ and $\sigma_{\rm eff}$ seen in Fig. 10.

Because the *total* (luminous + dark) mass, $M_{\rm tot,dyn}$, is well constrained by the dynamical models (inside the region with kinematical data), a spurious increase in the luminous mass component would be accompanied by a corresponding decrease in the nominal dark matter fraction, $f_{\rm DM,dyn}$, of the models. More specifically, under the assumption $M_{\rm tot,dyn} = M_{\rm tot,gal}$, the model parameters ($\Upsilon_{*,\rm dyn}$, $f_{\rm DM,dyn}$) and the actual galaxy parameters ($\Upsilon_{*,\rm gal}, f_{\rm DM,gal}$) would be related via

$$\Upsilon_{*,\rm dyn} = \Upsilon_{*,\rm gal} + (f_{\rm DM,gal} - f_{\rm DM,dyn})\,\Upsilon_{\rm tot,dyn}, \tag{7}$$

where $\Upsilon_{\rm tot,dyn} \equiv M_{\rm tot,dyn}/L$ is the total mass-to-light ratio (including dark matter). A degeneracy in the mass decomposition (at fixed *total* mass) would therefore correlate the offset

$$\Delta\Upsilon \equiv \frac{\Upsilon_{*,\rm dyn} - \Upsilon_{*,\rm gal}}{\Upsilon_{\rm Krou}} \tag{8}$$

in stellar mass-to-light ratios with the offset

$$\Delta f_{\rm DM} \equiv f_{\rm DM,dyn} - f_{\rm DM,gal} \tag{9}$$

in dark matter fractions as

$$\Delta\Upsilon = -\frac{\Upsilon_{\rm tot,dyn}}{\Upsilon_{\rm Krou}}\,\Delta f_{\rm DM}. \tag{10}$$

Fig. 15(a) shows $\Upsilon_{*,\rm dyn}/\Upsilon_{\rm Krou}$ against the models' dark matter fractions $f_{\rm DM,dyn}$ (inside $r_{\rm eff}$). There is a slight trend for $\Upsilon_{*,\rm dyn}/\Upsilon_{\rm Krou}$ to be particularly large whenever $f_{\rm DM,dyn}$ is low. Note that an intrinsic dark matter variation from galaxy to galaxy at a constant IMF scatters galaxies horizontally in Fig. 15(a), while an IMF variation at constant dark matter fraction scatters galaxies vertically. The luminous–dark matter degeneracy discussed above scatters galaxies along the arrow shown in Fig. 15(a). It marks the direction along which the fitted ($\Upsilon_{*,\rm dyn}$, $f_{\rm DM,dyn}$) are expected to separate from the galaxies' ($\Upsilon_{*,\rm gal}, f_{\rm DM,gal}$) according to equation (10) and – for each galaxy – depends on the ratio $\Upsilon_{\rm tot,dyn}/\Upsilon_{\rm Krou}$. For the arrow in Fig. 15(a), we have used the average $\langle\Upsilon_{\rm tot,dyn}/\Upsilon_{\rm Krou}\rangle = 2.39$ over the Coma sample. The distribution of the majority of Coma galaxies roughly follows the arrow, in particular, below $f_{\rm DM,dyn} \lesssim 0.3$.

Fig. 15(a) suggests, though does not unambiguously prove, that the scatter in $\Upsilon_{*,\rm dyn}/\Upsilon_{\rm Krou}$ could reflect a degeneracy in the dynamical mass decomposition. A contamination of some $\Upsilon_{*,\rm dyn}$ with

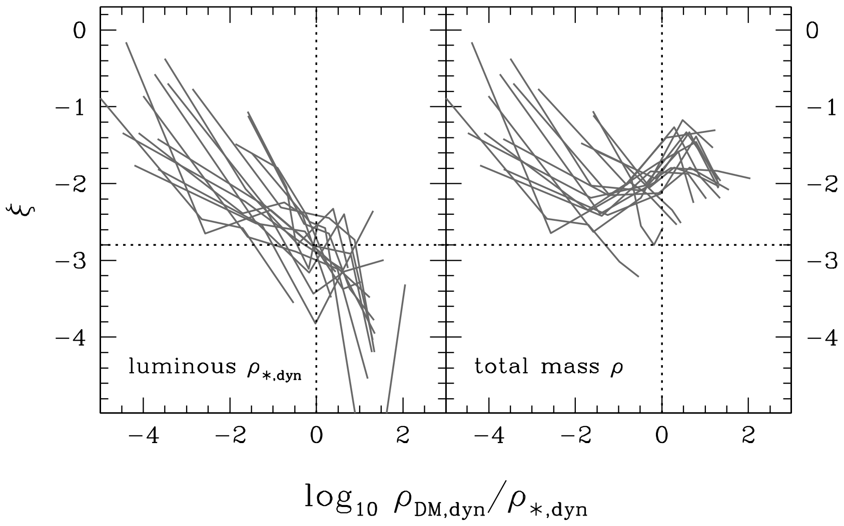

Figure 14. Comparison of the local logarithmic density slope $\xi = \mathrm{d}\ln\rho(r)/\mathrm{d}\ln(r)$ with the density ratio $\rho_{\mathrm{DM,dyn}}(r)/\rho_{*,\mathrm{dyn}}(r)$ of dark to luminous matter at the same radius. Left-hand panel: logarithmic slope of the luminous mass density $\rho_{*,\mathrm{dyn}} = \Upsilon_{*,\mathrm{dyn}} \times \nu$; right-hand panel: logarithmic slope of the total mass density $\rho = \Upsilon_{*,\mathrm{dyn}} \times \nu + \rho_{\mathrm{DM,dyn}}$. The vertical dotted lines indicate where luminous and dark matter equalize. To the left-hand side of these lines, the luminous mass dominates (inner regions of the galaxies) and to the right-hand side, dark matter dominates (outer regions of the galaxies). The horizontal lines are for $\xi = -2.8$, the luminous slope at which dark matter takes over luminous matter.

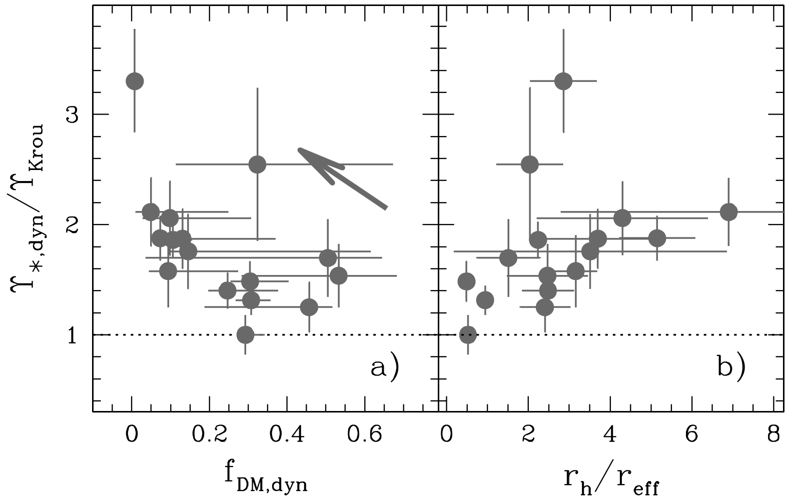

Figure 15. $\Upsilon_{*,\mathrm{dyn}}/\Upsilon_{\mathrm{Krou}}$ against the dark matter fraction $f_{\mathrm{DM,dyn}}$ (panel a) and against the halo core radius r_{h} (scaled by the effective radius r_{eff}; panel b). Shifting mass from the dark halo component into the luminous one at constant *total* mass moves galaxies along the direction indicated by the arrow in the left-hand panel (a). Note that for the right-hand panel, the galaxy GMP1990 has been omitted, since its dark matter fraction is so low that the determination of a halo core radius becomes meaningless.

dark matter would also explain the trend seen in Fig. 15(b), where $\Upsilon_{*,\mathrm{dyn}}/\Upsilon_{\mathrm{Krou}}$ is plotted against the halo core radius r_{h} (in units of r_{eff}). The more the inner dark matter goes into $\Upsilon_{*,\mathrm{dyn}}$, the less the model component $\rho_{\mathrm{DM,dyn}}$ traces the actual inner dark matter of the galaxies. Instead, it only represents the outer parts of the dark matter haloes. Correspondingly, one would expect relatively larger halo core radii (with respect to r_{eff}) whenever $\Upsilon_{*,\mathrm{dyn}}$ is large compared to Υ_{ssp} – as seen in Fig. 15(b).

Napolitano et al. (2010) analysed a large set of early-type galaxies with two-component spherical Jeans models and found dynamical $\Upsilon_{*,\mathrm{dyn}}$ close to the Salpeter IMF when using collisionless haloes from cosmological simulations without baryon contraction. However, their $\Upsilon_{*,\mathrm{dyn}}$ get closer to the Kroupa IMF when the baryonic contraction is taken into account. Baryonic contraction might therefore be one way to make luminous and dark matter distributions similar enough to explain the difference between $\Upsilon_{*,\mathrm{dyn}}$ and Υ_{Krou} (see Section 5.4).

In our modelling approach, the halo parameters are allowed to vary freely, without being connected to results from cosmological simulations. On the one hand, this ensures that the baryonic contraction is implicitly taken into account: the best-fitting models for more contracted haloes are simply expected to occur in a different region of parameter space. On the other hand, the steepest halo density profiles that we probed are those from cosmological simulations without the baryon contraction (NFW haloes; cf. Section 2.1). If the actual galaxy halo profiles are steeper, then the best-fitting dynamical model would still be obtained by shifting some fraction of the inner dark mass into $\Upsilon_{*,\mathrm{dyn}}$.

More similar distributions of luminous and dark matter in some galaxies than in others could also reflect differences in their evolutionary histories. For example, the cosmological simulations of Naab, Johansson & Ostriker (2009) indicate a difference in the radial distribution of *in situ* formed stars relative to stars that were accreted during mergers. *In situ* formed stars have a more centrally concentrated radial distribution than stars that were accreted in collisionless mergers. The latter dominate the stellar mass density around $r_{\rm eff}$. In any case, more detailed investigations of numerical simulations are required to reach a conclusion related to a possible degeneracy between luminous and dark matter in the inner regions of galaxies.

5.3 The distribution of dark matter in case of a universal Kroupa IMF

If we adopt the point of view that the stellar IMF in early-type galaxies is universal and Kroupa like, then this affects the distribution of dark matter significantly. The reason is that in this case our nominal halo component captures only a part of the galaxies' dark matter, while a large fraction follows the light and is included in $\Upsilon_{*,\rm dyn}$. In fact, a universal Kroupa IMF implies the dark matter fractions, $f_{\rm DM,Krou}$, to read

$$f_{\rm DM,Krou}(r) \equiv f_{\rm DM,dyn}(r) + \frac{(\Upsilon_{*,\rm dyn} - \Upsilon_{\rm Krou}) \times L(r)}{M_{\rm tot,dyn}(r)}. \tag{11}$$

These fractions are larger than the nominal $f_{\rm DM,dyn}$ derived from $\rho_{\rm DM,dyn}$, have a smaller scatter and slightly increase with the galaxy $\sigma_{\rm eff}$ (cf. Fig. 16).

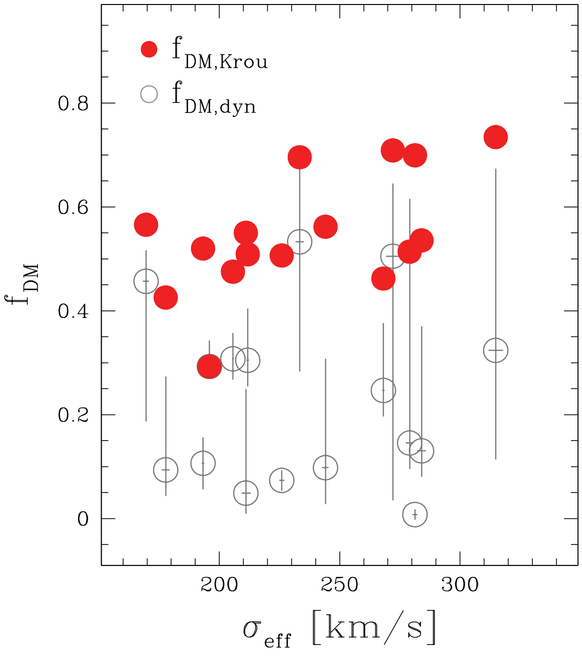

Figure 16. Dark matter fractions (inside the effective radius $r_{\rm eff}$) against velocity dispersion $\sigma_{\rm eff}$. Open circles: fraction of dark matter, $f_{\rm DM,dyn}$, that does not follow the light; filled circles: dark matter fraction $f_{\rm DM,Krou}$ assuming (i) a universal Kroupa IMF; and (ii) that the excess mass $(\Upsilon_{*,\rm dyn} - \Upsilon_{\rm Krou}) \times \nu$ is a component of the dark matter that follows the light.

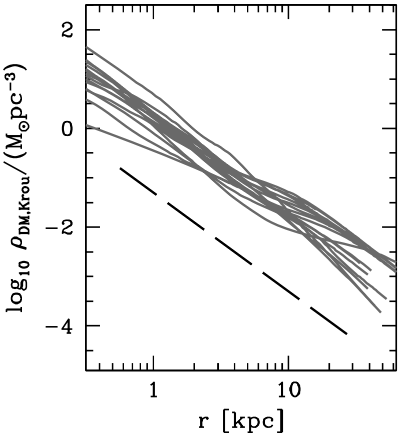

Figure 17. Spherically averaged dark matter density, $\rho_{\rm DM,Krou}$, against radius. The excess mass $(\Upsilon_{*,\rm dyn} - \Upsilon_{\rm Krou}) \times \nu$ with respect to a Kroupa IMF stellar population has been added to the dark matter halo. The dashed line indicates a power-law density with a logarithmic slope of −2.

Fig. 17 shows the spherically averaged dark matter density profiles

$$\rho_{\rm DM,Krou} \equiv \rho_{\rm DM,dyn} + (\Upsilon_{*,\rm dyn} - \Upsilon_{\rm Krou}) \times \nu, \tag{12}$$

including the extra dark matter required for a Kroupa IMF (cf. equation 2). These density profiles are smooth and close to a power law with the logarithmic slope slightly shallower than −2. The slight wiggles in the profiles around ≈5 kpc indicate the transition from the outer parts, which are dominated by $\rho_{\rm DM,dyn}$, to the inner parts, which are dominated by the second term on the right-hand side of equation (12).

5.4 Dark matter density and halo assembly epoch

In Thomas et al. (2009b), we estimated halo assembly epochs, $z_{\rm form}$, based on the assumption that the average dark matter density $\langle\rho_{\rm DM}\rangle$ inside $2r_{\rm eff}$ scales with $(1 + z_{\rm form})^3$. From the overdensity of dark matter in early-type galaxies relative to spiral galaxies, one can then narrow down elliptical galaxy assembly redshifts with an additional assumption about the typical formation redshift of spiral galaxies ($z_{\rm form} \approx 1$). Adopting a universal Kroupa IMF results in average dark matter densities a factor of ≈3 larger than the nominal ones of the dynamical models. The strongest contribution to this increase comes from the single galaxy GMP1990 which has a negligible $f_{\rm DM,dyn}$, but a large $\Upsilon_{*,\rm dyn}/\Upsilon_{\rm Krou}$. Without this galaxy, dark matter densities are only larger by about a factor of 1.6, which allows the halo assembly redshifts to increase from $z_{\rm form} \approx 1$–3 (Thomas et al. 2009b) to about $z_{\rm form} \approx 1.5$–3.5.

As a second test, we have compared the $\rho_{\rm DM,Krou}$ from Fig. 17 directly to the galaxy formation models of De Lucia & Blaizot (2007). These models do not include the dynamical reaction of dark matter on the baryon infall. Therefore, we first subtracted from the observed dark matter profile, $\rho_{\rm DM,Krou}$, the expected effect of baryon contraction by assuming the adiabatic approximation (i.e. by inverting the equations of Blumenthal et al. 1986). The relationship between the average dark matter density and halo formation redshift in the models of De Lucia & Blaizot (2007) is well fitted by $\log\langle\rho_{\rm DM}\rangle \approx -2.9 + \log(1 + z_{\rm form})^3$. We used this relation to calculate Coma galaxy assembly redshifts from the decontracted Kroupa dark matter halo densities. Fig. 18 shows that these halo assembly redshifts cover a similar range ($z_{\rm form} \approx 1$–3) to the ones obtained through the comparison with spiral galaxy dark matter densities. Note that we here computed star formation redshifts from the average stellar ages inside $r_{\rm eff}$, while in Thomas

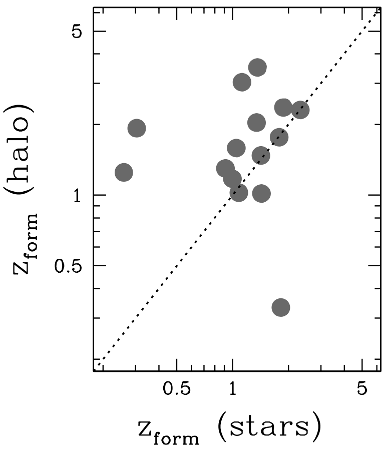

Figure 18. Star formation epoch (x-axis) against halo assembly epoch (y-axis). The dotted line represents the one-to-one relation.

et al. (2009b) we used the central stellar ages from Mehlert et al. (2003).

For many of the Coma galaxies, star formation redshifts and dark halo assembly redshifts are similar. Two galaxies appear far to the left-hand side of the one-to-one relation. These are GMP0756 and GMP1176, which have extended and relatively young ($\tau \approx 3$ Gyr) stellar discs. The galaxy on the bottom right-hand side, where the stars seem significantly older than the halo is GMP5568. As discussed in Thomas et al. (2009b), dry mergers can move galaxies below the one-to-one relation in Fig. 18. Besides this possibility, the effective radius of GMP5568 is exceptionally large ($r_{\rm eff} \approx 27$ kpc). Therefore, the dark matter density refers to a spatial region significantly larger than in any of our other Coma galaxies. If the effective radius of this galaxy was overestimated, then the average dark matter density would be underestimated and so would be the halo assembly redshift. This could also explain the high dark matter fraction of GMP5568 (cf. Table 1), since it generally increases with the physical distance from the galaxy centre.

6 THE TILT OF THE FUNDAMENTAL PLANE

The effective radius $r_{\rm eff}$, mean surface brightness $\langle I \rangle_{\rm eff}$ inside $r_{\rm eff}$ and the central velocity dispersion σ_0 of a galaxy are connected via

$$\sigma_0^2 = c_M \frac{GM}{r_{\rm eff}}, \tag{13}$$

where M is the total mass and

$$\langle I \rangle_{\rm eff} = \frac{L}{2\pi r_{\rm eff}^2}, \tag{14}$$

where L is the total luminosity. In virial equilibrium, the structure coefficient c_M depends on the orbital structure and the radial distributions of the mass and the tracer population. For a homologous family of dynamical objects, c_M is a constant and with $\langle \Upsilon \rangle \equiv M/L$, equations (13) and (14) lead to

$$\log \frac{r_{\rm eff}}{\rm kpc} = 2 \log \frac{\sigma_0}{\rm km\,s^{-1}} - \log \frac{\langle I \rangle_{\rm eff}}{\rm L_\odot\,pc^{-2}} + \gamma \tag{15}$$

and

$$\gamma = -\log \frac{\langle \Upsilon \rangle}{\rm M_\odot / L_{\mathit{R},\odot}} - \log \left(2\pi \frac{G}{\rm (km\,s^{-1})^2\,kpc\,M_\odot^{-1}} c_M \right). \tag{16}$$

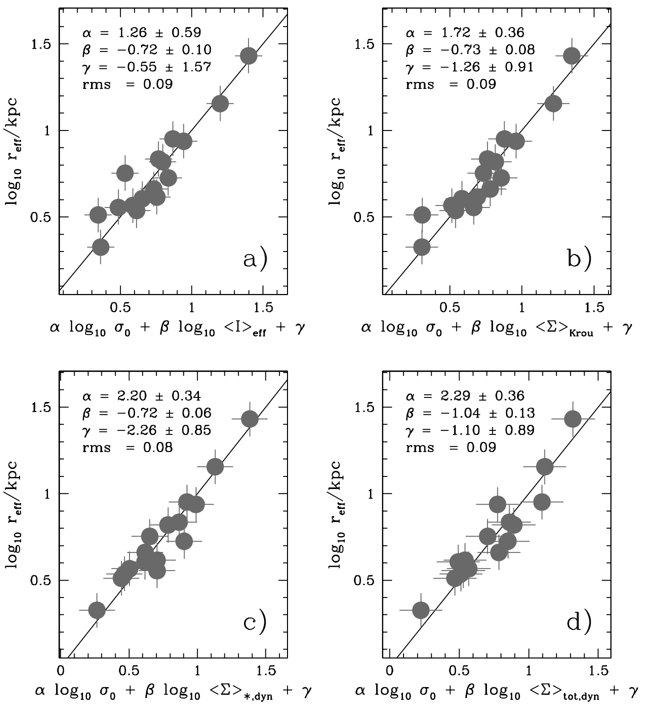

Figure 19. FP and MP of 16 Coma galaxies. In each panel, the best-fitting parameters of an orthogonal fit and the rms scatter in $\log r_{\rm eff}$ are quoted. Panel (a): traditional FP; panel (b): MP from stellar populations, that is, the effective surface brightness $\langle I \rangle_{\rm eff}$ is replaced by the mass density $\langle \Sigma \rangle_{\rm eff} \equiv \Upsilon_{\rm Krou} \times \langle I \rangle_{\rm eff}$; panel (c): same as panel (b) but for the dynamically derived stellar population $\Upsilon_{*,\rm dyn}$: $\langle \Sigma \rangle_{*,\rm dyn} \equiv \Upsilon_{*,\rm dyn} \times \langle I \rangle_{\rm eff}$; and panel (d): same as panel (c), but instead of the dynamically derived *stellar* mass-to-light ratio the *total* $M_{\rm tot,dyn}/L$ (including dark matter) is used: $\langle \Sigma \rangle_{\rm tot,dyn} \equiv M_{\rm tot,dyn}/L \times \langle I \rangle_{\rm eff}$ ($M_{\rm tot,dyn}/L$ is taken at the effective radius). The solid lines trace the one-to-one relation.

The actually observed FP (Djorgovski & Davis 1987; Dressler et al. 1987) of early-type galaxies reads

$$\log \frac{r_{\rm eff}}{\rm kpc} = \alpha \log \frac{\sigma_0}{\rm km\,s^{-1}} + \beta \log \frac{\langle I \rangle_{\rm eff}}{\rm L_\odot\,pc^{-2}} + \gamma \tag{17}$$

with $\alpha \neq 2$ and $\beta \neq -1$. It is tilted with respect to the virial plane of equation (15).

Fig. 19(a) shows the FP[2] of Coma galaxies. The best-fitting parameters of an orthogonal fit are $\alpha = 1.26 \pm 0.58$ and $\beta = -0.72 \pm 0.10$ (bootstrap errors). Within the statistical uncertainties, the fit is consistent with the r-band FP of SDSS early-type galaxies ($\alpha = 1.49 \pm 0.05$, $\beta = -0.75 \pm 0.01$; Bernardi et al. 2003; Hyde & Bernardi 2009). The larger errors result from the smaller sample size. Most of the difference with respect to Bernardi et al. (2003) goes back to four galaxies (GMP0144, GMP0756, GMP1176 and GMP5975) that are distinct from the rest of the sample in several respects: (1) they have young central stellar cores ($\tau_0 < 7$ Gyr; cf. Mehlert et al. 2003); (2) at least two of them have an extended thin stellar disc; and (3) they follow different dark halo scaling relations (Thomas et al. 2009b). Fig. 20 is equivalent to Fig. 19 except that these four galaxies have been removed. The corresponding FP matches well with the SDSS results.

---

[2] Note that in this section we use the average velocity dispersion σ_0 inside the central 2 arcsec, derived in the same way as the effective $\sigma_{\rm eff}$ discussed in Section 3.

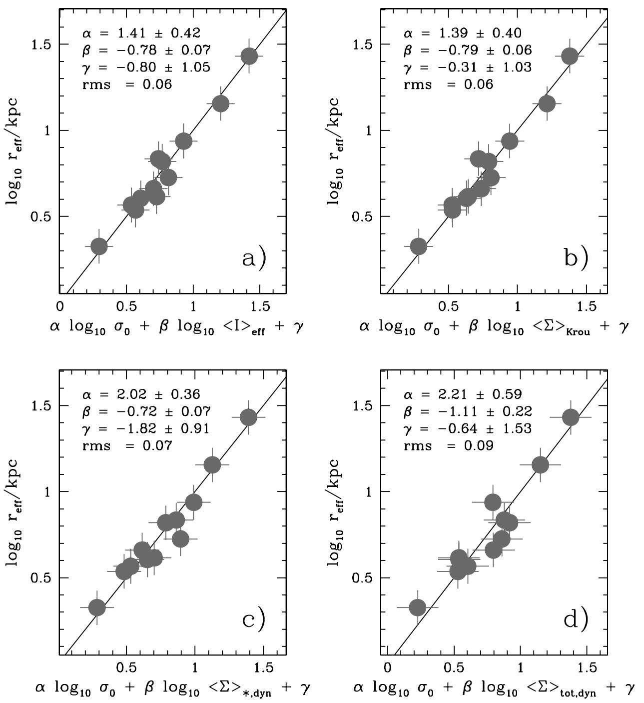

Figure 20. Same as Fig. 19, but four galaxies with young stellar cores are omitted.

6.1 The fundamental mass plane

The tilt in the FP can reflect non-homology (i.e. c_M being a function of the galaxy mass) or variations in $\langle\Upsilon\rangle$ (or both). A systematic variation in $\langle\Upsilon\rangle$, in turn, could reflect stellar population effects or changes in the dark matter distribution. In any case, the dynamical models allow to incorporate variations of $\langle\Upsilon\rangle$ into the FP. For this purpose, let $\langle\Sigma\rangle_{\rm eff}$ denote the average surface mass density inside $r_{\rm eff}$. Then, equation (17) can be written as

$$\log\frac{r_{\rm eff}}{\rm kpc} = \alpha\log\frac{\sigma_0}{\rm km\,s^{-1}} + \beta\log\frac{\langle\Sigma\rangle_{\rm eff}}{\rm M_\odot\,pc^{-2}} + \gamma, \tag{18}$$

where

$$\gamma = -\log\left(2\pi\frac{G}{({\rm km\,s^{-1}})^2\,{\rm kpc\,M_\odot^{-1}}}c_M\right). \tag{19}$$

Equation (18) defines the so-called fundamental mass plane (MP; Bolton et al. 2007).

Figs 19(b)–(d) show Coma galaxy MPs for different choices of $\langle\Sigma\rangle_{\rm eff}$. Using either $\langle\Sigma\rangle_{\rm Krou} \equiv \Upsilon_{\rm Krou}\times\langle I\rangle_{\rm eff}$ (panel b) or $\langle\Sigma\rangle_{*,\rm dyn} \equiv \Upsilon_{*,\rm dyn}\times\langle I\rangle_{\rm eff}$ (panel c), the tilt is reduced, but does not vanish ($\beta \neq -1$). The change in α from Fig. 19(a) to Fig. 19(b) is consistent with the SDSS analysis of Hyde & Bernardi (2009). Fig. 19(d) shows the case of $\langle\Sigma\rangle_{\rm eff}$, including all the projected mass (luminous and dark) inside $r_{\rm eff}$. The MP of Fig. 19(d) is tilt-free within the errors. The match to the virial plane of equation (15) improves further when omitting the four galaxies harbouring young stellar cores (cf. Fig. 20). With $\langle\Upsilon\rangle \equiv M_{\rm tot,dyn}/L$, the MP has the same scatter as the FP itself (cf. Figs 19a and d). For the subsample of old Coma galaxies, the scatter slightly increases (cf. Fig. 20).

6.2 The tilt of the Fundamental Plane

The tilt in the FP is reduced when the effective surface brightness is replaced by an effective surface mass derived from $\Upsilon_{\rm ssp}$.[3] The amount of reduction is consistent with the SDSS results of Hyde & Bernardi (2009). In accordance with Graves & Faber (2010), the tilt is further reduced if $\Upsilon_{\rm ssp}$ is replaced by the dynamical $\Upsilon_{*,\rm dyn}$. As discussed above, the different scalings of $\Upsilon_{*,\rm dyn}$ and $\Upsilon_{\rm ssp}$ with $\sigma_{\rm eff}$ could reflect (1) changes in the IMF; or (2) changes in the distribution of dark matter. The absence of any correlation between $\Upsilon_{*,\rm dyn}/\Upsilon_{\rm Krou}$ and stellar population parameters makes (2) more likely than (1). Finally, the tilt vanishes completely (for a subsample of Coma galaxies with uniformly old stellar populations), if the remaining dark mass inside the effective radius $r_{\rm eff}$ is taken into account as well. This behaviour is also found in lensing studies (Bolton et al. 2007).

In our FP analysis, we have not tried to calculate c_M directly from the dynamical models. However, the density distribution (in particular the galaxy flattening) as well as the orbital structure vary among the Coma galaxies (Thomas et al. 2009a). Nevertheless, Fig. 20(d) indicates that for old Coma early types the tilt of the FP is dominated by mass-to-light ratio effects rather than any possible variation in c_M.

6.3 Mass estimators

Wolf et al. (2010) provide an estimation for the mass

$$M_{\rm W10}(r_3) = \frac{3\langle\sigma^2\rangle r_3}{G} \tag{20}$$

inside the radius r_3 where the logarithmic density slope of the tracer population is $\xi = -3$. Here, $\langle\sigma^2\rangle$ is the average of the projected σ^2 over the whole galaxy. Wolf et al. (2010) derived equation (20) for non-rotating spherical galaxies. For the Coma galaxies, we averaged the measured σ^2 up to $r_{\rm eff}$, ignoring the galaxies' rotation velocities. Fig. 21(a) compares Coma galaxy masses, $M_{\rm tot,dyn}(r_3)$, against the predictions of equation (20). Averaged over all Coma galaxies, we find $\langle M_{\rm tot,dyn}(r_3)/M_{\rm W10}(r_3)\rangle = 1.03 \pm 0.27$ (rms scatter). Fig. 21(b) is similar to Fig. 21(a), except for the additional approximation $r_3 \approx r_{1/2} \approx 4/3 r_{\rm eff}$, where $r_{1/2}$ is the deprojected half-light radius. The agreement with the Coma galaxies is still very good.

Fig. 22 compares luminous dynamical masses with the estimator

$$M_{\rm C06} = \frac{5\sigma_{\rm eff}^2 r_{\rm eff}}{G} \tag{21}$$

from Cappellari et al. (2006). When using luminous dynamical masses, $M_{*,\rm dyn} = \Upsilon_{*,\rm dyn}\times L$, from model fits that do have a separate dark matter component, we find $\langle M_{*,\rm dyn}/M_{\rm C06}\rangle = 0.86 \pm 0.35$ (cf. Fig. 22a). The small offset disappears if we use model fits that do not have an additional dark matter component (equivalent to the approximation made in Cappellari et al. 2006). The corresponding luminous dynamical masses, $M_{*,\rm sc} = \Upsilon_{*,\rm sc}\times L$ (cf. Table 1), are slightly larger and the comparison with equation (21) yields $\langle M_{*,\rm sc}/M_{\rm C06}\rangle = 1.01 \pm 0.36$ (cf. Fig. 22). The rms scatter includes both the measurement errors and the anisotropy variations (Thomas et al. 2007b). Note, however, that the assumption that all the mass follows the light is inconsistent with lensing masses (cf. Fig. 5).

---

[3] In Section 6, the surface mass was derived from the Kroupa IMF, but the difference between the Kroupa and Salpeter IMFs is only a constant scaling factor. The results for the Salpeter IMF are therefore similar.

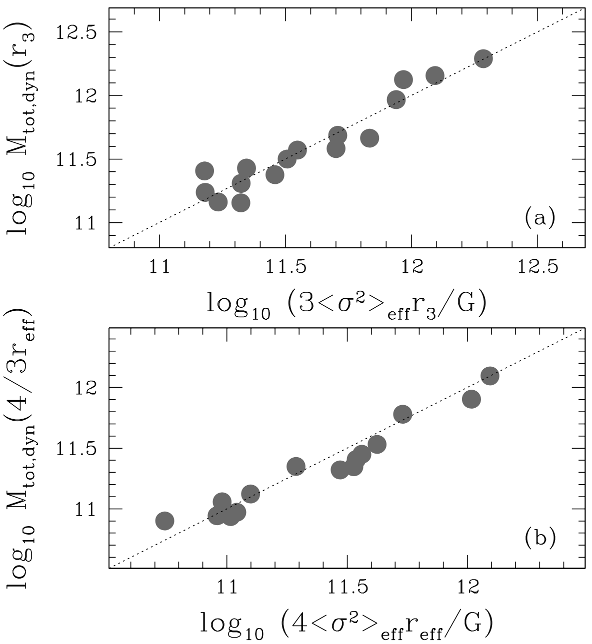

Figure 21. Comparison of Coma galaxies with the Wolf et al. (2010) mass estimator (cf. equation 20): panel (a) – total dynamical mass enclosed inside the radius r_3, where the logarithmic slope of the luminosity distribution equals $\xi = -3$; and panel (b) – similar to panel (a) but with the additional approximation $r_3 \approx 4/3 r_{\rm eff}$.

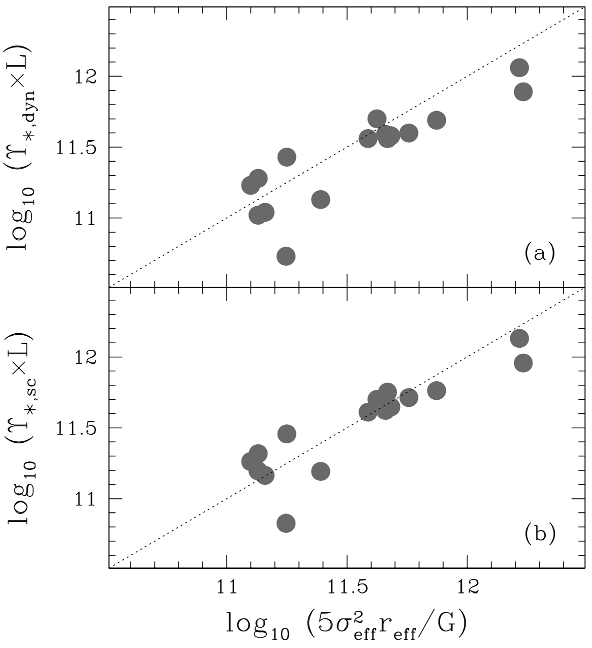

Figure 22. Comparison of Coma galaxies with the Cappellari et al. (2006) virial mass estimator (cf. equation 21): panel (a) – luminous dynamical mass, $\Upsilon_{*,\rm dyn} \times L$, from fits explicitly allowing for a separate component of dark matter; and panel (b) – luminous dynamical mass, $\Upsilon_{*,\rm sc} \times L$, from fits assuming that all the mass follows the light.

Thus, the Wolf et al. (2010) formula gives good estimates for the *total* dynamical mass inside a radius which is a bit larger than $r_{\rm eff}$. The virial estimator of Cappellari et al. (2006) captures the entire dynamical mass that results under the assumption that the *total mass follows light*. Assuming $r_3 \approx r_{1/2}$, equation (21) implies

$$M_{\rm C06}(r_3) \approx M_{\rm C06}(r_{1/2}) = \frac{M_{\rm C06}}{2} = \frac{2.5\sigma_{\rm eff}^2 r_{\rm eff}}{G}, \qquad (22)$$

whereas from equation 20 and $r_3 \approx 4/3 r_{\rm eff}$, it follows that

$$M_{\rm W10}(r_3) \approx \frac{4\langle\sigma^2\rangle r_{\rm eff}}{G}. \qquad (23)$$

Concerning the enclosed mass inside $4/3 r_{\rm eff}$, the two mass estimators would differ by a factor of $4/2.5 = 1.6$, unless $\langle\sigma^2\rangle \neq \sigma_{\rm eff}^2$. Due to the different treatment of rotation, $\sigma_{\rm eff}^2 \approx 1.3\,\langle\sigma^2\rangle$ in the Coma sample such that the actual difference is only about 20 per cent.

7 SUMMARY

We compared dynamically derived stellar mass-to-light ratios, $\Upsilon_{*,\rm dyn}$, with completely independent results from simple stellar population models. Our dynamical models are based on Schwarzschild's orbit superposition technique and have two mass components. One follows the light and its mass-to-light ratio, $\Upsilon_{*,\rm dyn}$, is assumed to approximate the stellar mass distribution. The other mass component explicitly accounts for dark matter. This way, any potential degeneracy between the stellar mass and the dark matter halo is minimized. The Coma galaxy sample studied here is currently the largest with axisymmetric Schwarzschild models including dark matter explicitly.

Intrinsic uncertainties in the modelling, in particular related to the assumption of axial symmetry, are unlikely to bias our results significantly. The main reason is that in projection our dynamical masses match well with completely independent results from strong gravitational lensing.

Our main findings are as follows:

(i) For galaxies with low velocity dispersions ($\sigma_{\rm eff} \approx 200\,{\rm km\,s^{-1}}$), the assumption that all the mass follows the light yields projected masses larger than in comparable strong gravitational lens systems.

(ii) In high-velocity-dispersion galaxies ($\sigma_{\rm eff} \approx 300\,{\rm km\,s^{-1}}$), the assumption that mass follows light is consistent with strong lensing results.

(iii) Two-component dynamical models with an explicit dark halo component yield total projected masses that are in good agreement with results from strong gravitational lensing for all galaxies.

(iv) In two-component models, the mass-to-light ratio, $\Upsilon_{*,\rm dyn}$, of the component that follows the light increases with the galaxy velocity dispersion $\sigma_{\rm eff}$.

(v) Stellar population mass-to-light ratios, $\Upsilon_{\rm ssp}$ (for any fixed IMF), are largely independent of $\sigma_{\rm eff}$. As a result, the ratio $\Upsilon_{*,\rm dyn}/\Upsilon_{\rm ssp}$ of the luminous dynamical mass to stellar population mass increases with the galaxy velocity dispersion.

(vi) The luminous dynamical $\Upsilon_{*,\rm dyn}$ is always larger than, or at least equalizes, the stellar population mass-to-light ratio $\Upsilon_{\rm Krou}$ for a Kroupa IMF.

(vii) There is no correlation between $\Upsilon_{*,\rm dyn}/\Upsilon_{\rm ssp}$ and the stellar population age, metallicity or [α/Fe] ratio.

(viii) Inside $r_{\rm eff}$, the average fraction of dark matter (that does not follow the light) is $f_{\rm DM,dyn} = 23 \pm 17$ per cent in the Coma galaxies.

(ix) The tilt of the FP reduces if the effective surface brightness $\langle I\rangle_{\rm eff}$ is replaced by the stellar population surface mass density $\Upsilon_{\rm ssp} \times \langle I\rangle_{\rm eff}$, is further reduced if $\langle I\rangle_{\rm eff}$ is replaced by the dynamical stellar surface mass density $\Upsilon_{*,\rm dyn} \times \langle I\rangle_{\rm eff}$ and, for a subsample of galaxies with uniformly old stellar populations, vanishes completely with the *total* dynamical surface mass density $\langle \Sigma_{\mathrm{tot,dyn}} \rangle_{\mathrm{eff}}$.

(x) Commonly used mass estimators are accurate to the 20–30 per cent level.

The implications of these findings are as follows:

(i) That the luminous dynamical masses increase more rapidly with the galaxy velocity dispersion than stellar population masses for a fixed IMF could be due to a change in the IMF or due to an increasing amount of dark matter following a spatial distribution similar to that of the light.

(ii) If the IMF changes, then massive early types ($\sigma_{\mathrm{eff}} \approx 300\,\mathrm{km\,s^{-1}}$) have up to two times more stellar mass per stellar light than lower mass galaxies ($\sigma_{\mathrm{eff}} \approx 200\,\mathrm{km\,s^{-1}}$), which are consistent with a Kroupa IMF. However, the lack of any correlation between $\Upsilon_{*,\mathrm{dyn}}/\Upsilon_{\mathrm{ssp}}$ and the stellar population age, metallicity or [α/Fe] ratio is consistent with, though does not prove, that the IMF is actually universal.

(iii) If the IMF is universal, then the increase in luminous dynamical masses must primarily come from a component of dark matter that follows the light very closely and is more important in more massive galaxies. The IMF would be consistent with being Kroupa in all early types.

(iv) Independent of the actual slope of the stellar IMF, luminous dynamical masses are *on average* more accurately predicted by assuming a Salpeter IMF: $\langle \Upsilon_{*,\mathrm{dyn}}/\Upsilon_{\mathrm{Salp}} \rangle = 1.15$, but these masses may not represent exclusively stars. The Kroupa IMF yields $\langle \Upsilon_{*,\mathrm{dyn}}/\Upsilon_{\mathrm{Krou}} \rangle = 1.8$.

(v) Adopting a Kroupa IMF and counting the excess mass $(\Upsilon_{*,\mathrm{dyn}} - \Upsilon_{\mathrm{Krou}}) \times L$ as dark matter that follows the light doubles the average dark matter fractions inside r_{eff} to about $f_{\mathrm{DM,Krou}} \approx 55 \pm 12$ per cent. Moreover, it yields a smooth trend between the resulting $f_{\mathrm{DM,Krou}}$ and galaxy velocity dispersion and, also, smooth dark matter halo profiles.

(vi) The FP tilt is not a pure stellar population effect. Further inferences about the tilt depend on the interpretation of the observed $\Upsilon_{*,\mathrm{dyn}}/\Upsilon_{\mathrm{Krou}}$. As above, that the tilt reduces when considering the dynamical mass $\Upsilon_{*,\mathrm{dyn}} \times L$ that follows the light could be due to (1) variations in the relative distribution of luminous and dark matter or (2) IMF variability.

ACKNOWLEDGMENTS

We thank the referee, Glenn van de Ven, for useful comments that helped us to improve the presentation of the results. JT acknowledges the financial support by the DFG through SFB 375 ‘Astro-Teilchenphysik’. RPS acknowledges the support by the DFG Cluster of Excellence ‘Origin and Structure of the Universe’. EMC is supported by the University of Padua through grants 60A02-1283/10 and CPDA089220, and by the Ministry of Education, University, and Research through grant EARA 2004-2006. SS acknowledges the support by the TR33 ‘The Dark Universe’ and by the Cluster of Excellence ‘Origin and Structure of the Universe’. The new Coma galaxy *HST* observations were obtained through the programme HSTGO-10884.0-A which was provided by the National Aeronautics and Space Administration (NASA) through a grant from the Space Telescope Science Institute, which is operated by the Association of Universities for Research in Astronomy, Inc., under NASA contract NAS5-26555. Funding for the SDSS and SDSS-II has been provided by the Alfred P. Sloan Foundation, the Participating Institutions, the National Science Foundation, the US Department of Energy, the NASA, the Japanese Monbukagakusho, the Max Planck Society and the Higher Education Funding Council for England. The SDSS website is http://www.sdss.org/. The SDSS is managed by the Astrophysical Research Consortium for the Participating Institutions. The Participating Institutions are the American Museum of Natural History, Astrophysical Institute Potsdam, University of Basel, University of Cambridge, Case Western Reserve University, University of Chicago, Drexel University, Fermilab, Institute for Advanced Study, Japan Participation Group, Johns Hopkins University, Joint Institute for Nuclear Astrophysics, Kavli Institute for Particle Astrophysics and Cosmology, Korean Scientist Group, Chinese Academy of Sciences (LAMOST), Los Alamos National Laboratory, Max-Planck-Institute for Astronomy, Max-Planck-Institute for Astrophysics, New Mexico State University, Ohio State University, University of Pittsburgh, University of Portsmouth, Princeton University, United States Naval Observatory and University of Washington.

REFERENCES

Auger M. W., Treu T., Bolton A. S., Gavazzi R., Koopmans L. V. E., Marshall P. J., Bundy K., Moustakas L. A., 2009, ApJ, 705, 1099
Barnabè M., Czoske O., Koopmans L. V. E., Treu T., Bolton A. S., Gavazzi R., 2009, MNRAS, 399, 21
Barnabe M., Czoske O., Koopmans L. V. E., Treu T., Bolton A. S., 2011, preprint (arXiv:1102.2261)
Bender R., Burstein D., Faber S. M., 1992, ApJ, 399, 462
Bernardi M. et al., 2003, AJ, 125, 1866
Blumenthal G. R., Faber S. M., Flores R., Primack J. R., 1986, ApJ, 301, 27
Bolton A. S., Burles S., Treu T., Koopmans L. V. E., Moustakas L. A., 2007, ApJ, 665, L105
Cappellari M. et al., 2006, MNRAS, 366, 1126
Ciotti L., D’Ercole A., Pellegrini S., Renzini A., 1991, ApJ, 376, 380
Ciotti L., Lanzoni B., Renzini A., 1996, MNRAS, 282, 1
Corsini E. M., Wegner G., Saglia R. P., Thomas J., Bender R., Thomas D., 2008, ApJS, 175, 462
David L. P., Forman W., Jones C., 1991, ApJ, 369, 121
De Lucia G., Blaizot J., 2007, MNRAS, 375, 2
Djorgovski S., Davis M., 1987, ApJ, 313, 59
Dressler A., Lynden Bell D., Burstein D., Davies R. L., Faber S. M., Terlevich R., Wegner G., 1987, ApJ, 313, 42
Ferreras I., Saha P., Leier D., Courbin F., Falco E. E., 2010, MNRAS, 409, L30
Gebhardt K. et al., 2003, ApJ, 583, 92
Gerhard O., Kronawitter A., Saglia R. P., Bender R., 2001, AJ, 121, 1936
Godwin J. G., Metcalfe N., Peach J. V., 1983, MNRAS, 202, 113
Graves G. J., Faber S. M., 2010, ApJ, 717, 803
Grillo C., Gobat R., 2010, MNRAS, 402, L67
Hyde J. B., Bernardi M., 2009, MNRAS, 396, 1171
Kochanek C. S., 1991, ApJ, 373, 354
Koopmans L. V. E., Treu T., Bolton A. S., Burles S., Moustakas L. A., 2006, ApJ, 649, 599
Kroupa P., 2001, MNRAS, 322, 231
Maraston C., 1998, MNRAS, 300, 872
Maraston C., 2005, MNRAS, 362, 799
Maraston C., Strömbäck G., Thomas D., Wake D. A., Nichol R. C., 2009, MNRAS, 394, L107
Matsushita K., 2001, ApJ, 547, 693
Mehlert D., Saglia R. P., Bender R., Wegner G., 2000, A&AS, 141, 449
Mehlert D., Thomas D., Saglia R. P., Bender R., Wegner G., 2003, A&A, 407, 423
Naab T., Johansson P. H., Ostriker J. P., 2009, ApJ, 699, L178
Napolitano N. R., Romanowsky A. J., Tortora C., 2010, MNRAS, 405, 2351
Navarro J. F., Frenk C. S., White S. D. M., 1996, ApJ, 462, 563
Renzini A., Ciotti L., 1993, ApJ, 416, L49
Richstone D. O., Tremaine S., 1988, ApJ, 327, 82
Saglia R. P., Bender R., Dressler A., 1993, A&A, 279, 75

Saglia R. P. et al., 2010, A&A, 509, A61
Salpeter E. E., 1955, ApJ, 121, 161
Scalo J. M., 1986, Proc. IAU Symp. 116, Luminous Stars and Associations in Galaxies. Reidel, Dordrecht, p. 451
Schwarzschild M., 1979, ApJ, 232, 236
Thomas J., 2006, PhD thesis, LMU Munich
Thomas D., Greggio L., Bender R., 1999, MNRAS, 302, 537
Thomas D., Maraston C., Bender R., 2003, MNRAS, 339, 897
Thomas J., Saglia R. P., Bender R., Thomas D., Gebhardt K., Magorrian J., Richstone D., 2004, MNRAS, 353, 391
Thomas J., Saglia R. P., Bender R., Thomas D., Gebhardt K., Magorrian J., Corsini E. M., Wegner G., 2005a, MNRAS, 360, 1355
Thomas D., Maraston C., Bender R., Mendes de Oliveira C., 2005b, ApJ, 621, 673
Thomas J., Jesseit R., Naab T., Saglia R. P., Burkert A., Bender R., 2007a, MNRAS, 381, 1672
Thomas J., Saglia R. P., Bender R., Thomas D., Gebhardt K., Magorrian J., Corsini E. M., Wegner G., 2007b, MNRAS, 382, 657
Thomas J. et al., 2009a, MNRAS, 393, 641
Thomas J., Saglia R. P., Bender R., Thomas D., Gebhardt K., Magorrian J., Corsini E. M., Wegner G., 2009b, ApJ, 691, 770
Treu T., Auger M. W., Koopmans L. V. E., Gavazzi R., Marshall P. J., Bolton A. S., 2010, ApJ, 709, 1195
Trujillo I., Burkert A., Bell E. F., 2004, ApJ, 600, L39
van de Ven G., Mandelbaum R., Keeton C. R., 2009, MNRAS, 398, 607
van Dokkum P., Conroy C., 2010, Nat, 468, 940
van Dokkum P., Conroy C., 2011, preprint (arXiv:1102.3431)
Wegner G., Corsini E. M., Saglia R. P., Bender R., Merkl D., Thomas D., Thomas J., Mehlert D., 2002, A&A, 395, 753
Wolf J., Martinez G. D., Bullock J. S., Kaplinghat M., Geha M., Muñoz R. R., Simon J. D., Avedo F. F., 2010, MNRAS, 406, 1220
York D. G. et al., 2000, AJ, 120, 1579

This paper has been typeset from a TEX/LATEX file prepared by the author.